


## Article

# Effect of a Radially Offset Impeller on the Unsteady Characteristics of Internal Flow in a Double-Suction Centrifugal Fan

Zhiyun Chen <sup>1</sup>, Hui Yang <sup>1</sup>, Yikun Wei <sup>1</sup> , Haijiang He <sup>2</sup>, Chenyu Zhang <sup>2</sup>, Tiehua Nie <sup>2</sup>, Peiquan Yu <sup>3</sup> and Wei Zhang <sup>1,\*</sup> 

- <sup>1</sup> Key Laboratory of Fluid Transmission Technology of Zhejiang Province, Zhejiang Sci-Tech University, Hangzhou 310018, China  
<sup>2</sup> Zhejiang Yilida Ventilator Co., Ltd., Taizhou 318056, China  
<sup>3</sup> National Fan Product Quality Inspection and Testing Center (Zhejiang), Shaoxing 312000, China  
\* Correspondence: zhangwei@zstu.edu.cn

**Abstract:** The impeller of double-suction centrifugal fans may be radially offset from the centerline of the volute due to faults in assembly or installation. The radial offset results in the more significant non-uniformity of internal flow in the centrifugal fan, which is biased from the designed condition, and deteriorates the aerodynamic performances of the fan. In this paper, we performed Unsteady Reynolds-averaged Navier–Stokes (URANS) simulations on the unsteady internal flow of a double-suction centrifugal fan. The impeller of the fan is offset in the radial direction from its original position and is thus closer to the wall of the volute on one side and away from the opposite side. Numerical results show that the offset impeller changes the size of the gap between the impeller and collector in the radial direction, which produces a non-uniform distribution of static pressure and even reversed flow at the inlet of the impeller. As the impeller is offset away from the baffle of the volute, reversed flow back into the volute is observed, and strong circulating vortices form around the baffle, which weakens the diffusing capability of the volute. However, as the impeller is offset close to the baffle, the internal flow of the volute generally improves the flow patterns within the impeller, while the boundary layer separates from the pressure surface of the blades near the front disc as the flow angle varies; the maximum velocity of reversed flow could reach 20 m/s which lowers the efficiency of the fan.

**Keywords:** centrifugal fan; offset impeller; numerical simulation; pressure fluctuation



**Citation:** Chen, Z.; Yang, H.; Wei, Y.; He, H.; Zhang, C.; Nie, T.; Yu, P.; Zhang, W. Effect of a Radially Offset Impeller on the Unsteady Characteristics of Internal Flow in a Double-Suction Centrifugal Fan. *Processes* **2022**, *10*, 1604. <https://doi.org/10.3390/pr10081604>

Academic Editors: Jin-Hyuk Kim, Joon Ahn, Sung-Min Kim, Lei Tan, Ji Pei and Bin Huang

Received: 14 July 2022

Accepted: 10 August 2022

Published: 13 August 2022

**Publisher's Note:** MDPI stays neutral with regard to jurisdictional claims in published maps and institutional affiliations.



**Copyright:** © 2022 by the authors. Licensee MDPI, Basel, Switzerland. This article is an open access article distributed under the terms and conditions of the Creative Commons Attribution (CC BY) license (<https://creativecommons.org/licenses/by/4.0/>).

## 1. Introduction

The impeller is the only working component of a centrifugal fan that converts mechanical energy to the kinetic energy of air. The geometry of the impeller is critical to the aerodynamic performances of the centrifugal fan, and a lot of effort is devoted to optimization [1]. Most of the current research on the design and optimization of centrifugal fans mainly focuses on the geometry of the blade and the volute in which the air moves within and interacts. Li et al. [2] studied the effect of the enlargement of the impeller on the performance of the fan, and the results proved that the larger impeller increases the total pressure but lowers the efficiency. Younsi et al. [3] conducted experimental and numerical studies on an impeller with four different geometric parameters using the same volute and analyzed the effects of factors such as irregular blade spacing, blade count, and radial distance between the impeller periphery, and the volute tongue on the performance of the fan. Ding et al. [4] established five impeller models with different blade installation angles and found that appropriately increasing the outlet installation angle would increase fan efficiency and reduce impeller noise. Song et al. [5] studied the influence of different staggered angles of two blades of a double-suction centrifugal pump on volute's pressure

fluctuations and axial flow. Liu et al. [6] studied the influence of a straight shroud with different inclined angles on fan performance. The results showed that, within a reasonable range of inclination, the selection of the straight shroud simplifies fan manufacturing and improves fan performance, and the dynamic balance of the impeller and aerodynamic performance still meet certain requirements. Jiang et al. [7] adopted the design of an impeller with unevenly spaced blades, which effectively reduce noise without affecting aerodynamic performance. Madhwesh et al. [8] improved fan efficiency by optimizing the front and rear shroud fences of the impeller of a backward-swept centrifugal fan. Ye et al. [9] adopted a bevel cutting design on the blade to change the inlet geometry, leading to a more uniform flow distribution and reducing impact loss, vortex loss, and drag loss.

The characteristics of internal flow within the centrifugal fan are greatly dependent on the patterns of inflow as a result of the interaction between the impeller and collector [10]. The collector is implemented to ensure that the air enters the impeller smoothly and uniformly; thus, the energy loss is reduced, and the aerodynamic efficiency is enhanced. However, the radially offset impeller changes the gap between the impeller and the collector. A larger gap causes gap leakage and reduces the efficiency of the fan [11,12]. Zhu et al. [13] studied the influence of the depth of the impeller inserted into the collector on the aerodynamic performance of a small centrifugal fan. The analysis results showed that gap leakage is positively correlated with the insertion depth of the impeller, and the aerodynamic performance of the ventilator can be significantly improved by reducing the insertion depth of the collector under the designed and large flow rates. Fukutomi et al. [14] experimentally studied the influence of the eccentric position of two collectors on the pressure coefficient and the internal flow of the fan. It is found that as the eccentric position is located far upstream of the volute outlet, the pressure coefficient is significantly higher than that without eccentricity. Liu et al. [15] proposed an asymmetric D-type collector. The research showed that the collector can effectively suppress the backflow phenomenon at the inlet of the collector near the volute tongue under low-flow conditions, and that the performance of the fan is significantly improved.

The characteristics of the internal flow of the fan are also determined by the geometry of the volute and its relative position with respect to the impeller [16]. The radially offset impeller changes the distance from the outlet of the impeller to the wall of the volute, thereby affecting the patterns of the internal flow of the volute. The centrifugal fan and volute were optimized by Pan et al. [17]. Detailed internal flow data under designed and off-designed flow conditions showed that enlarging the flow passage area near the tongue region, while without changing the exit–inlet area ratio of the volute, leads to an improvement in the internal flow distribution at off-design flow conditions. Yang et al. [18] designed a test device with adjustable installation positions of the impeller and volute to study the effects of different installation positions of the impeller and volute on fan performance. It is found that the position where the center of the impeller coincides with the geometric center of the volute is not the best. The appropriate relative installation position could improve the fan's efficiency at the design speed and reduce noise. Wang et al. [19] conducted a numerical study on the aerodynamic effects of impeller–diffuser axial misalignment in a low-flow-coefficient centrifugal compressor. The results show that the flow, especially near the diffuser inlet, is influenced by axial misalignment. Daniel et al. [20] found an optimum relative position of the impeller and volute where the efficiency is maximized and the resultant radial force is minimized at the design flow coefficient. By assembling a circular volute pump with the appropriate impeller relative to the volute position, the design simplicity of a circular volute can be utilized without compromising pump hydraulic performance or radial force characteristics, as compared to a typical spiral volute. Younsi et al. [21] studied the interactions and unsteadiness induced by rotating blades relative to the volute and their impact on the aero-acoustic behavior of the fan. A correlation between wall pressure fluctuations and far-field noise signals has been found. Ding et al. [22] studied the effect of different volute openness on the aerodynamic characteristics of a centrifugal fan. The increased volute openness improves the flow in the impeller channel, makes the outlet

more uniform, and decreases mixing loss. Li et al. [23] studied the origins and effects of complex vortical structures near the volute outlet of a multi-blade centrifugal fan. The streamlines are divided into two parts, i.e., backflow and outflow, at the volute outlet. A numerical study of the aerodynamic and aero-acoustic behaviors of a backward curved blade centrifugal fan was conducted under two important flow conditions by Zhang et al. [24]. The aero-acoustic simulation results showed that the volute noise is much larger than the blade noise, and the noise is mainly propagated from the outlet duct of the fan.

The volute tongue of the centrifugal fan prevents air from circulating in the volute; thus, the air at the impeller outlet has a strong impact on the volute tongue. The noise in this area is regarded as one of the main aerodynamic noise sources of the multi-blade centrifugal fan [25]. Meanwhile, the radial gap between the impeller outlet and the volute tongue also has a great influence on the internal pressure fluctuation of the rotating machinery [26,27]. Lv et al. [28] simulated flow in a fan with different radial relative positions, and the optimal central location of the fan impeller was obtained. The baseline fan and the modified fan with the optimized central location of the impeller were comparably analyzed, which showed that the optimized fan enhances the radial adaptive internal flow under designed and variable conditions. Patil et al. [29] focused on the effect of varied volute tongue clearance on the performance of backward-curved blade centrifugal blowers. The results showed that volute tongue clearance has a significant effect on the performance of the centrifugal blower, and these parameters increase with a decrease in volute tongue clearances. Jin et al. [30] studied the effect of the gap between the impeller and the volute tongue on the performance and pressure fluctuation of a double suction pump. They found that with the increase in the gap between the impeller and the volute tongue, the head is reduced, but the efficiency increases, and the pressure fluctuation decreases.

The literature reviewed above discussed the characteristics of the internal flow of a centrifugal fan with consideration of the influences from the offset impeller and the variable size of the gap between the impeller and the collector or volute tongue. The results showed that the size of the gap affects the uniformity and unsteadiness of inflow, and thus determines the patterns of internal flow of the fan, and the aerodynamic and aero-acoustic performances are affected. For an industrial double-suction centrifugal fan, the impeller is installed within the volute under the constraints of supports outside the volute, and there could be minor misalignment between the centerlines of the impeller and volute; thus, the impeller is radially offset within the volute and is not right behind the collector. The inflow of the impeller is circumferentially non-uniform, which further affects the internal flow of the volute. In this paper, we performed a numerical investigation of the influence of the offset impeller on the characteristics of the internal flow of a double-suction centrifugal fan model. An impeller that is offset in the radial direction is considered to have positive and negative offset distances, i.e., in opposite directions. The flow in the collector, impeller, volute, and outflow duct is analyzed in detail, and the distributions of velocity and pressure and their fluctuations, the vertical structures, and the near-wall flow on the solid surfaces are studied. The results and conclusions could provide a reference to the aerodynamic design, installation practice, and maintenance of similar types of fans.

## 2. Numerical Setup

### 2.1. Fan Model

The present work focused on a double-suction centrifugal fan with backward-swept blades. Figure 1a shows the baseline model of the fan. The impeller with 12 blades on each side is placed within the volute, and their axial centerlines coincide. The air moves into the impeller through the collector, exits from the impeller to the volute, and then is led out of the fan from the outlet section, where a V-shape baffle is installed. The computational domain consists of the fan, two inflows, and one outflow sub-domain representing the motion of air, as shown in Figure 1b. To ensure the full development of inflow and outflow, the length of the inflow and outflow ducts is five times the outlet diameter of the fan. The specifications of the centrifugal fan are given in Table 1.

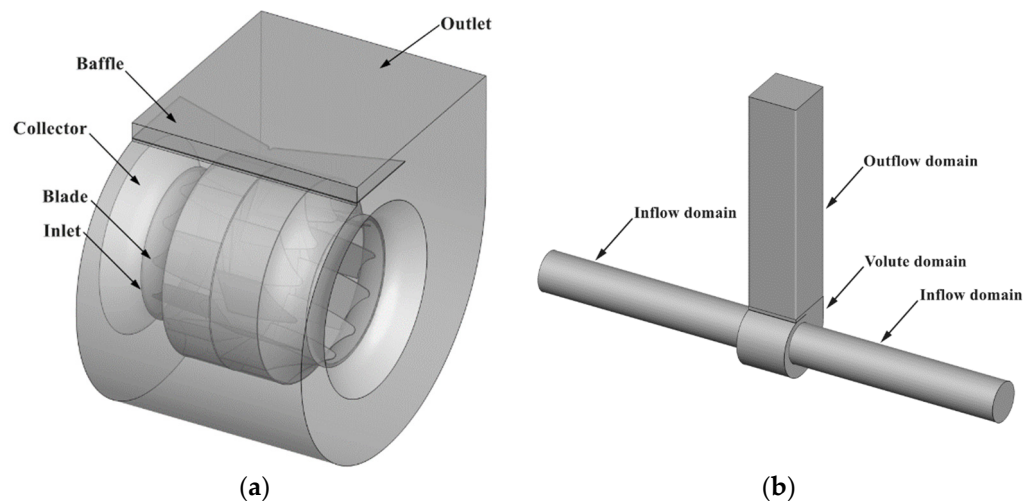


**Figure 1.** Model of the centrifugal fan and computational domain. (a) impeller and volute; (b) computational domain.

**Table 1.** Specifications of the centrifugal fan.

Parameters	Value
Flow rate, $Q_n$ ( $\text{m}^3/\text{h}$ )	9670
Rotation speed of fan $n$ , (rpm)	1800
Diameter of impeller inlet, $d$ (mm)	327
Diameter of impeller outlet, $D$ (mm)	466
Impeller height, $L$ (mm)	158
Number of blades, $Z$	24

The radially offset impeller on the centrifugal fan is schematically shown in Figure 2. The impeller in red ( $X = 0$  mm) denotes the baseline model, where the axial centerlines of the impeller and volute coincide. The impeller in green ( $X = -5$  mm) and blue ( $X = +5$  mm) represents the radially offset ones; the offset distance is 5 mm, and the direction is strictly perpendicular to the outflow. All three models, including the baseline and modified models with an offset impeller, have the same geometrical parameters, except for the relative position of the impeller and volute. The offset impeller causes uneven radial clearance between the collector and the inlet of the impeller, which affects the circumferential uniformity of flow at the inlet of the impeller. The openness of the volute and the relative clearance between the impeller and the baffle also change, which affects the exiting flow from the impeller and outflow from the fan.

## 2.2. Numerical Methods

### 2.2.1. Governing Equations and Turbulence Models

Air is the working medium of the centrifugal fan. Since the velocity of air in the low-pressure industrial fan is normally low, with a Mach number less than 0.3, the flow is incompressible and is governed by the conservation equations of mass and momentum:

$$\frac{\partial u_i}{\partial x_i} = 0 \quad (1)$$

$$\frac{\partial u_i}{\partial t} + u_j \frac{\partial u_i}{\partial x_j} = f_i - \frac{1}{\rho} \frac{\partial P^*}{\partial x_i} + \nu \frac{\partial^2 u_i}{\partial x_j \partial x_j} \quad (2)$$

where  $x_i$  is the components of the Cartesian coordinate system;  $u_i$  is the velocity component;  $P^*$  represents the pressure considering the conversion of turbulent kinetic energy and centrifugal force;  $f_i$  is the component of volume force.

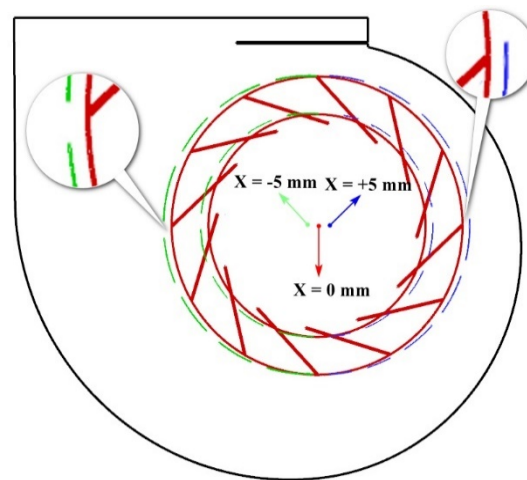


**Figure 2.** Schematic diagram of the offset impeller. The center of the impeller is placed at  $X = 0$  mm for the baseline model and  $X = \pm 5$  mm for the modified models.

In this paper, there is a large range of strong shear flows on the surface of the blade, which makes it easy to produce flow separation. Therefore, the SST  $k$ - $\omega$  turbulence model [31] is employed in the numerical simulation, which considers the effect of the free shear layer on turbulent viscosity and has good prediction capability in the near-wall and far-field regions [32]. In addition, this model takes into account the influence of turbulent principal shear stress transport and can accurately simulate the adverse pressure gradient flow field with high accuracy and reliability. The SST  $k$ - $\omega$  turbulence model is applied to compute the turbulent viscosity. The transport equations of the turbulent kinetic energy  $k$  and the specific dissipation rate  $\omega$  of SST are: The  $k$  and  $\omega$  [33] equations in this model are:

$$\frac{\partial(\rho k)}{\partial t} + \frac{\partial(\rho U_i k)}{\partial x_i} = \tilde{P} - \beta^* \rho k \omega + \frac{\partial}{\partial x_i} \left[ (\mu + \sigma_k \mu_t) \frac{\partial k}{\partial x_i} \right] \quad (3)$$

$$\frac{\partial(\rho \omega)}{\partial t} + \frac{\partial(\rho U_i \omega)}{\partial x_i} = \alpha \rho S^2 - \beta \rho \omega^2 + \frac{\partial}{\partial x_i} \left[ (\mu + \sigma_\omega \mu_t) \frac{\partial \omega}{\partial x_i} \right] + 2(1 - F_1) \rho \sigma_{\omega 2} \frac{1}{\omega} \frac{\partial k}{\partial x_i} \frac{\partial \omega}{\partial x_i} \quad (4)$$

where the turbulent kinetic energy  $k$  and the specific dissipation rate  $\omega$  are respectively defined as:

$$k = \frac{1}{2} u'_i u'_i \quad (5)$$

$$\omega = \frac{\varepsilon}{k \beta^*} \quad (6)$$

where the blending function  $F_1$  is defined by:

$$F_1 = \tanh \left\{ \left\{ \min \left[ \max \left( \frac{\sqrt{k}}{\beta^* \omega y}, \frac{500\nu}{y^2 \omega} \right), \frac{4\rho \sigma_{\omega 2} k}{CD_{k\omega} y^2} \right] \right\}^4 \right\} \quad (7)$$

With

$$CD_{k\omega} = \max \left( \left( 2\rho \sigma_{\omega 2} \frac{1}{\omega} \frac{\partial k}{\partial x_i} \frac{\partial \omega}{\partial x_i}, 10^{-10} \right) \right)$$

and  $y$  is the distance to the nearest wall.

The model defines turbulent viscosity as:

$$\nu_t = \frac{a_1 k}{\max(a_1 \omega, SF_2)} \quad (8)$$

where  $S$  is the invariant measure of the strain rate, and  $F_2$  is a second blending function defined by:

$$F_2 = \tanh \left[ \left\{ \max \left( \frac{2\sqrt{k}}{\beta^* \omega y'}, \frac{500\nu}{\omega y^2} \right) \right\}^2 \right] \quad (9)$$

where  $\nu$  represents the kinematic viscosity, and  $y$  represents the wall-normal distance.

### 2.2.2. Numerical Methods

The whole computational domain is discretized by hybrid structured and unstructured grids, as shown in Figure 3. The inflow and outflow sub-domains are discretized by block-structured grids considering their geometrical simplicity, and the sub-domains of the impeller and volute are treated by unstructured grids. The grid is specifically refined on all solid walls to resolve the boundary layer flow. The number of grids in each sub-domain is given in Table 2. The grid refinement guarantees that the value of  $y^+$  on the surfaces of blade edge, hub, and shroud is normally  $y^+ < 30$  in most regions, while near the outlet of the impeller, the value could increase to about 90. The skewness value of the grid is less than 0.5. The sub-domain of the impeller is set as a rotational domain, while the rest of the sub-domains are set stationary.

We performed both steady and unsteady simulations using the RANS and URANS approaches. The simulations are carried out using the commercial software ANSYS-Fluent based on the finite volume method. The SIMPLER method has a skew correction function and good computational convergence, so it is used for pressure–velocity coupling. Because the second-order upwind scheme has high computational accuracy and stability, we used it to discretize other physical quantities. The boundary conditions of the two types of simulations are the same. A constant mass flow rate is prescribed at the inflow section of the upstream inflow tube, and zero-gauge pressure is employed at the outflow section of the outflow cavity. The no-slip condition is used for velocity components on all solid walls, and the standard wall function is used to resolve the turbulent boundary layer flow. The multi-reference-frame (MRF) model is used to treat the rotation of the fan, and the static coordinate system is used for inflow and outflow parts. The interface between the impeller, collector, and inlet pipe adopts the frozen rotor method.

We first perform the RANS simulation until the converged result with relative residual less than  $10^{-3}$  is obtained for the equations of mass, momentum, turbulent kinetic energy and turbulent dissipation rate. The result is then used as the initial condition to start the URANS simulation, and the simulation continues as the impeller rotates for 12 revolutions before the data are collected. The physical time step size is fixed as the impeller rotates for one degree; thus, 360 steps are required for one revolution of the impeller.

**Table 2.** Number of grids in each sub-domain.

Sub-Domain	Number of Grids ( $\times 10^3$ )
Impeller	4262
Inflow	1580
Outflow	2889
Volute	1588
Total	13,319

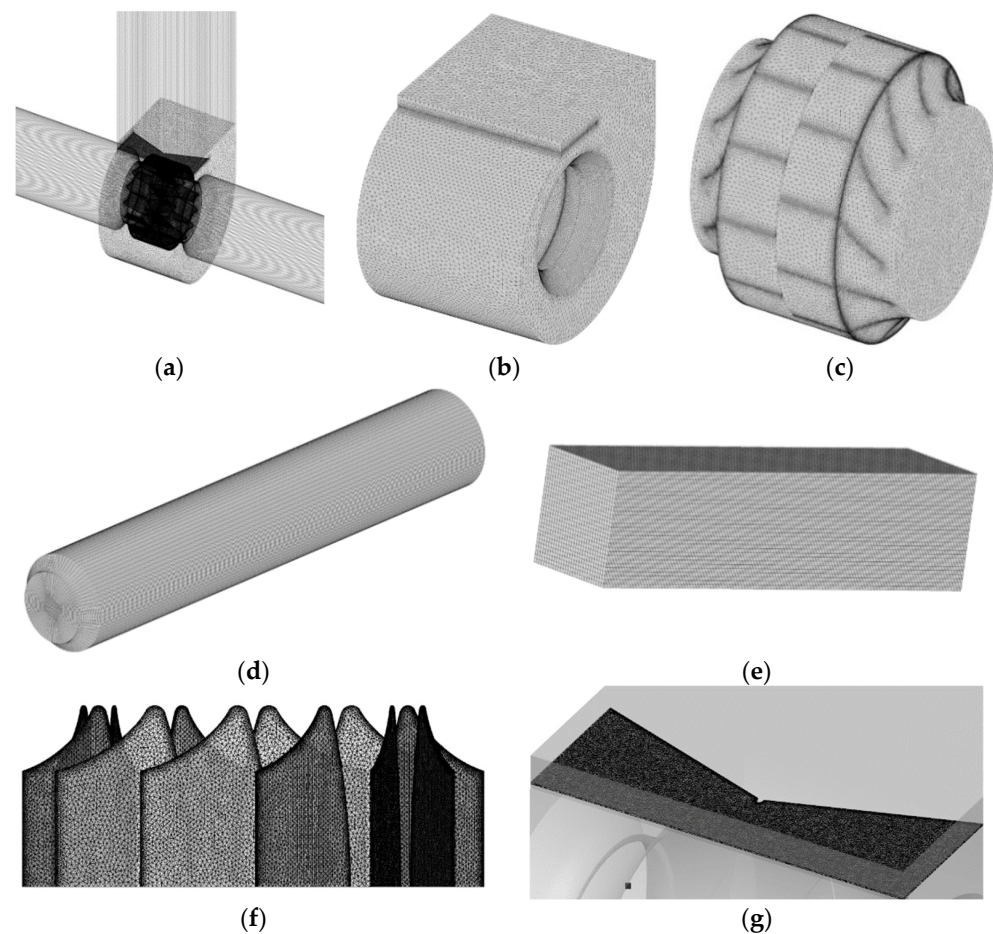


**Figure 3.** Schematic of the grid for the whole computational domain and various sub-domains: (a) the grid for the whole computational domain; (b) the grids of the volute; (c) the grids of the impeller; (d) the grids of the inlet; (e) the grids of the outlet; (f) the grids of the blades; (g) the grids of the baffle.

### 2.3. Grid Sensitivity Study

A grid sensitivity study was performed to identify the necessary number of grids to accurately resolve the internal flow of the centrifugal fan. The sensitivity study was conducted for a steady-state simulation of the internal flow of the fan under the designed flow rate  $9670.3 \text{ m}^3/\text{h}$ . As shown in Figure 4a, the static pressure rise, which is defined as the difference between the surface-averaged static pressure at the inlet and outlet of the fan, is chosen as an indication to represent the performance of the fan. Since the sub-domains of inflow, outflow, and volute are stationary and relatively simple in geometry, the grid is only varied in the impeller sub-domain. Five sets of grids are generated, with a total number of about 10.01, 11.52, 13.32, 15.52, and 20.72 million, respectively. The static pressure rise obtained under these grid sets is shown in Figure 4b. It is seen in the figure that as the grid number increases from 10.01 million to 11.52 million, the static pressure increases by 29 Pa, while a further refinement to 13.32 million gives an increase of 10 Pa. However, the 15.52 million grid could only provide another increase of 1 Pa, which is negligible considering the magnitude of the rise in static pressure. To balance the computational effort and accuracy, we employed 13.32 million for following URANS simulations.

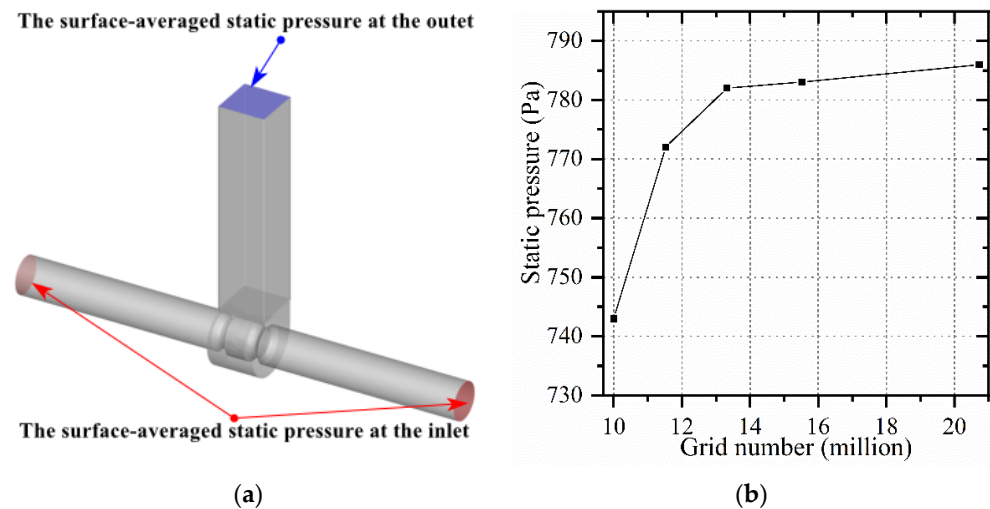


**Figure 4.** (a) The location of the surface-averaged static pressure at the inlet and outlet of the fan; (b) static pressure under different grid numbers.

### 3. Results and Discussion

#### 3.1. Aerodynamic Performances of the Fan

The static pressure rise and static pressure efficiency for the baseline and modified models are listed in Table 3. The modified models with radially offset impellers slightly lower both pressure rise and efficiency; the pressure rise is reduced by about 1.12% and 0.57% for the  $X = -5$  mm and  $X = +5$  mm models, and efficiency by 4.04% and 3.75%, respectively. This indicates that the offset impeller partially deteriorates the internal flow of the fan and induces more energy loss compared with the baseline model.

**Table 3.** Static pressure rise and static pressure efficiency for the baseline and modified models.

Method	Model	Static Pressure Rise (Pa)	Static Pressure Efficiency (%)
URANS	$X = -5$ mm	853.48	66.5
URANS	$X = 0$ mm	863.17	69.3
URANS	$X = +5$ mm	858.23	66.7

The time history of static pressure rise obtained by URANS is given in Figure 5 along with the time-averaged value. The curves are produced as the impeller rotates for 12 revolutions under the designed flow rate. During the first few revolutions, there could be a large deviation between the instantaneous and time-averaged values, while the instantaneous value gradually recovers and fluctuates around the time-averaged value as the impeller rotates and the internal flow adapts to the rotating impeller. Comparison among the three curves shows that the modified fan model with an impeller of  $X = +5$  mm amplifies the pressure fluctuation, which reflects the more unstable internal flow of the fan.

#### 3.2. Flow in the Impeller

The interval angle of each blade is  $30^\circ$ ; thus, the unsteady patterns of the internal flow of the fan are analyzed here at four moments within one revolution of the impeller. Moment T1 is selected as the starting moment of the 12th revolution of the impeller, and moments T2, T3, and T4 are selected as the impeller rotates for  $90^\circ$  (the angle between the three blade channels) successively.



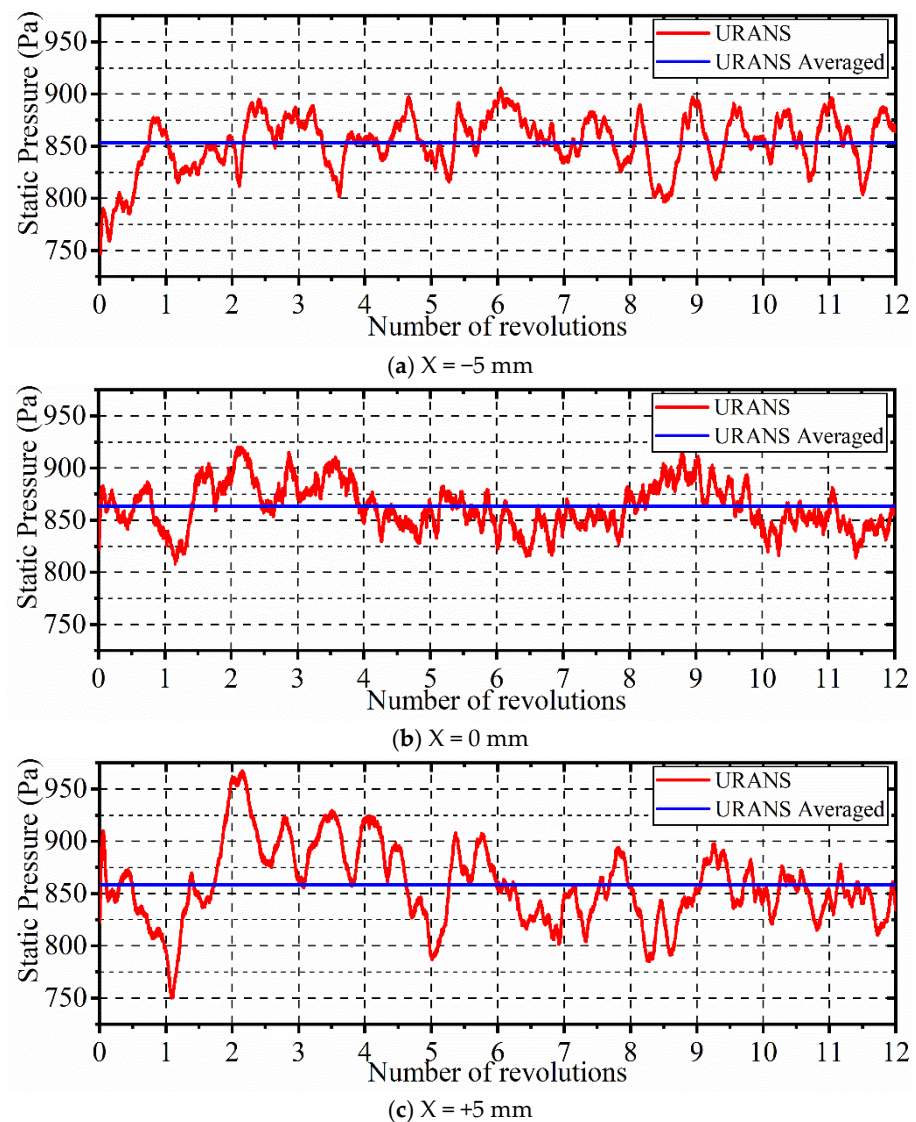


**Figure 5.** Time history of static pressure rise and its time-averaged value for the baseline and modified models.

### 3.2.1. Vortical Structures in Volute and Impellers

The vortical structures of internal flow within the fan are represented by the iso-surface of the  $Q$ -invariant at  $Q = 50,000$  and colored by the static pressure (static pressure in this paper is gauge pressure), as shown in Figure 6. Although the iso-surface at a constant magnitude only reflects a certain type of vortical structure and may miss others, it is still a powerful indicator of the shearing characteristics of the flow. It is seen in the figure that the iso-surface is notable in regions with drastic geometric variation, such as the blade passages, the near-wall regions of the volute, and around the baffle.

For the modified model with an offset impeller at  $X = -5$  mm, the effect of the baffle in blocking the backflow is weakened, which results in fewer vortices outside the baffle. The flow with low pressure almost occupies the whole blade passage and the region between the impeller and the baffle. For the baseline model, vortices appear only near the shroud and the leading edge of the blades, which indicates that the flow of the inside baffle is blocked due to the offset impeller, thereby affecting the aerodynamic performance of the fan. The vortices occupy the least area for the  $X = +5$  mm model in the blade passages and around the baffle, indicating that uniformity of flow is improved by the offset impeller to the interior of the volute compared with the baseline model. However, for this model, the vortices are significant, the pressure is higher near the interior side of the volute, and the

pressure is significantly higher than that in other models. This is attributed to the offset impeller, which reduces the distance from the shroud to the volute surface, leading the fluid to impinge on the volute surface.

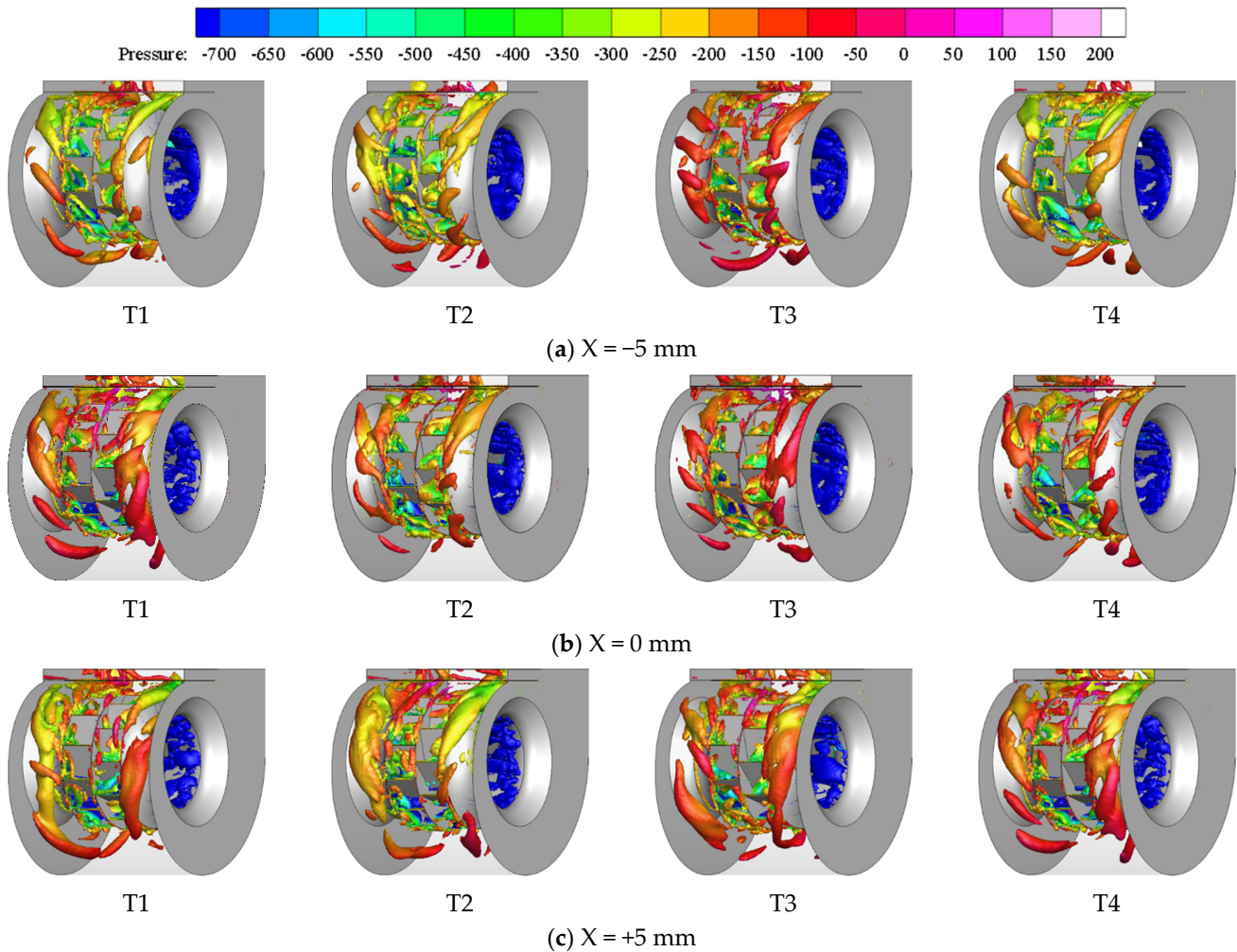


**Figure 6.** Iso-surface of  $Q = 50,000$  and colored by the static pressure.

### 3.2.2. Flow Patterns at the Inlet of Impeller

The distance between the collector and the inlet of impeller is changed by the radial offset of the impeller, which is anticipated to result in uneven distribution of pressure and velocity at the inlet of the impeller and consequently the internal flow of the impeller.

Figure 7 shows the distribution of instantaneous static pressure and the magnitude of axial velocity at the  $h = 5$  mm cross-section, which is given in Figure 8. It is seen that a low-pressure region is formed at the boundaries of the cross-section, and the magnitude of axial velocity exhibits quasi-concentric circles. For the baseline model ( $X = 0$  mm), the low-pressure region is the smallest in area, and the axial velocity is uniformly reduced in magnitude from the center to the boundary of the cross-section. For the modified model of  $X = -5$  mm, a large-scale low-pressure region and a small-scale high-pressure concentration area appear around the gap, and the position and area of the high- and low-pressure regions vary with the rotation of the impeller. The axial velocity presents an axisymmetric non-uniform distribution in which the magnitude is slightly higher in the high-pressure regions, and the distribution notably varies with the impeller rotation with changes of local magnitude. For the modified model of  $X = +5$  mm, the high- and low-pressure regions persist for almost the entire revolution of the impeller, and both regions rotate in time with the impeller. The magnitude of axial velocity changes in a large range; the iso-line of

$V = 14$  m/s originally located at the center of the impeller extends to the high-pressure region, making the low-speed region larger.

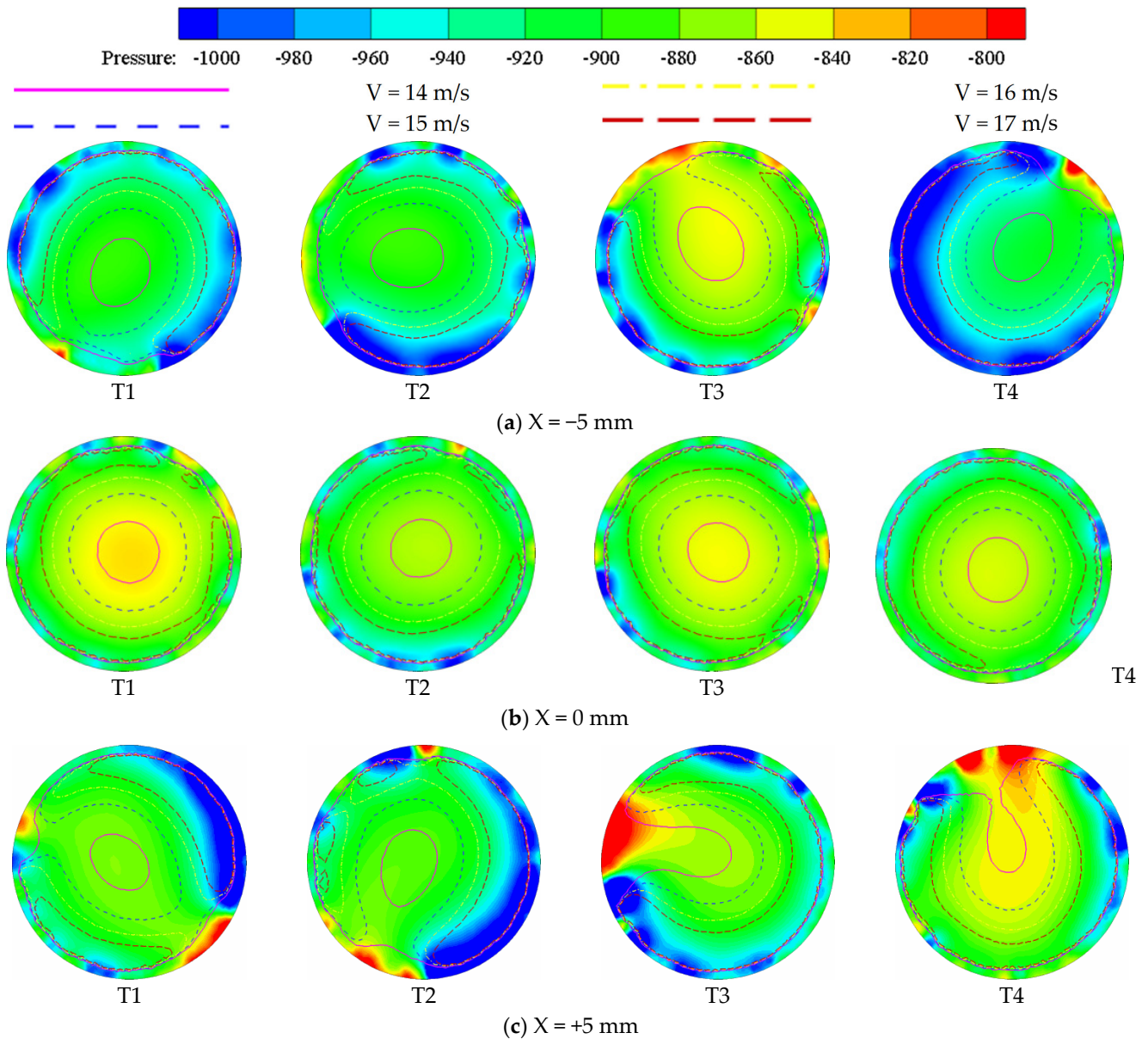


**Figure 7.** Distribution of static pressure and magnitude of axial velocity at the inlet cross-section of the impeller.

To further study the patterns of unsteady flow at the inlet of the impeller as affected by its radial offset, we explore the variation of axial velocity in the region of the inlet of the impeller. The axial velocity is extracted on three straight lines across the cross-section and through its center, as exhibited in Figure 8, with the  $h = 5$  mm line closest to the inlet and the  $h = 15$  mm line close to the leading edge of the blades.

The distribution of instantaneous axial velocity on several monitoring lines for the baseline and modified models is shown in Figure 9, where the negative velocity denotes reversed flow moving from the impeller to the collector. For the baseline model ( $X = 0$  mm), an M-shape velocity profile exists for flow obtained at different monitoring lines and at all moments; the axial velocity gradually increases from the center to the outside and reaches the maximum at  $L = \pm 150$  mm where the amplitude of local temporal fluctuation is the most obvious. The increased velocity at the boundary of the inlet cross-section, i.e., the gap

between the impeller and collector, results from the separated flow at the surface of the curved collector. Moreover, due to the gap between the impeller and collector, the fluid cannot move perfectly on the shroud after entering the impeller; thus, the velocity drops sharply to zero, and weak backflow occurs.

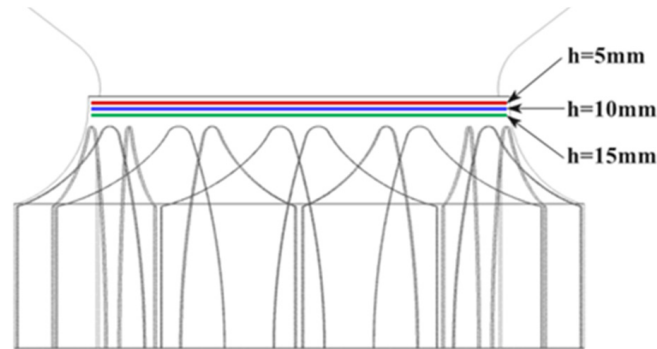


Figure 8. The positions of the three line probes around the inlet of the impeller.

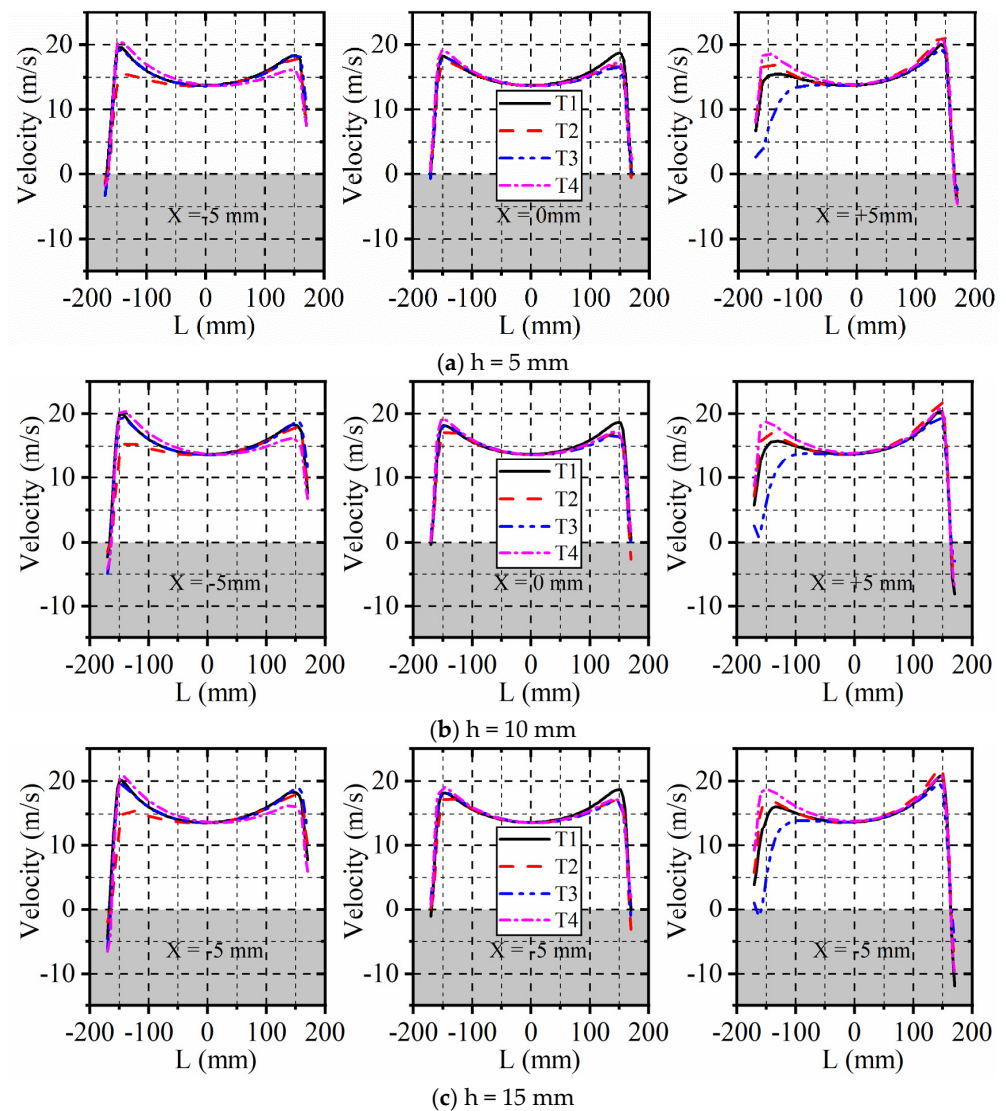


Figure 9. Distribution of axial velocity on the line probes at four moments.

The radial offset of the impeller leads to misalignment of the impeller and collector, increases the size of the gap between the shroud of the impeller and the collector on one side, and reduces on the other side, which could result in recirculating flow at the inlet of the impeller. This is attributed to the fact that the fluid cannot rapidly turn from the axial to radial direction after entering the impeller; thus, flow separation occurs on part of the interior surface of the shroud on which the incoming fluid impinges, and the magnitude of the velocity is relatively higher. Since the incoming fluid could enter the impeller without blockage by solid surfaces, the backflow disappeared. Due to the smaller gap, the axial velocity in this region varies significantly with time, and the unsteady characteristics are remarkable. However, for flow at the inlet cross-section of the impeller of the other side, where it is blocked by the collector, the incoming fluid cannot enter the impeller through the collector; thus, local recirculating flow is generated. As the fluid enters the impeller, the magnitude of the velocity of the reversed flow on this side is larger, indicating that the reversed flow occupies almost the whole inlet region of the impeller.

Comparing the axial velocities of the modified models at different moments, it is found that the velocity in the region  $L < -100$  mm changes significantly with time. This is because the fluid in this region is close to the outlet of the volute, and the fluid has experienced almost a full circle of acceleration of the impeller, resulting in high velocity. The reversed flow collides violently with the fluid entering the impeller, which makes the unsteady characteristics of this region remarkable. On the other hand, the inflow is stable. This shows that the change in the distance between the collector and the impeller inlet mainly causes an unstable change in the fluid velocity at the impeller inlet near the volute outlet.

### 3.2.3. Characteristics of Unsteady Flow Inside the Impeller

The unsteady and non-uniform flow at the inlet cross-section of the impeller propagates to the interior of the impeller. In this section, we analyze how the characteristics of the unsteady flow inside the impeller are affected by the offset impeller. We set three constant- $Y$  cross-sections to one side of the impeller with axial positions at  $Y = 2$  mm, 60 mm, and 118 mm, which are located near the central disc, at the middle of the impeller outlet, and near the shroud, as shown in Figure 10.

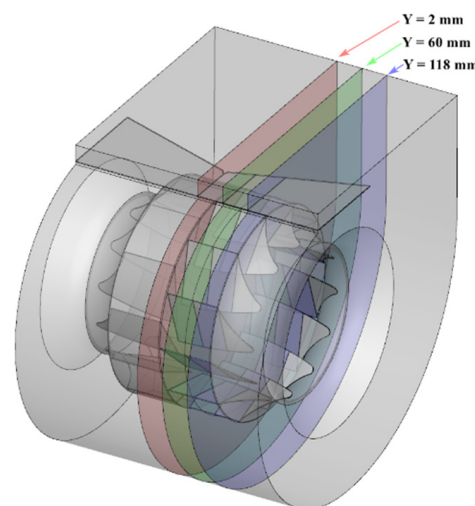


**Figure 10.** Schematic of the axial positions of the three constant- $Y$  cross-sections.

The distributions of instantaneous static pressure and streamlines on the  $Y = 2$  mm cross-section, i.e., near the central disc, are shown in Figure 11. There is almost no separation in the impeller for the baseline and modified models and at all moments, and the fluid exited from the impeller circulates within and leaves the volute smoothly. The offset impeller does not have a notable influence on flow near the central disc.

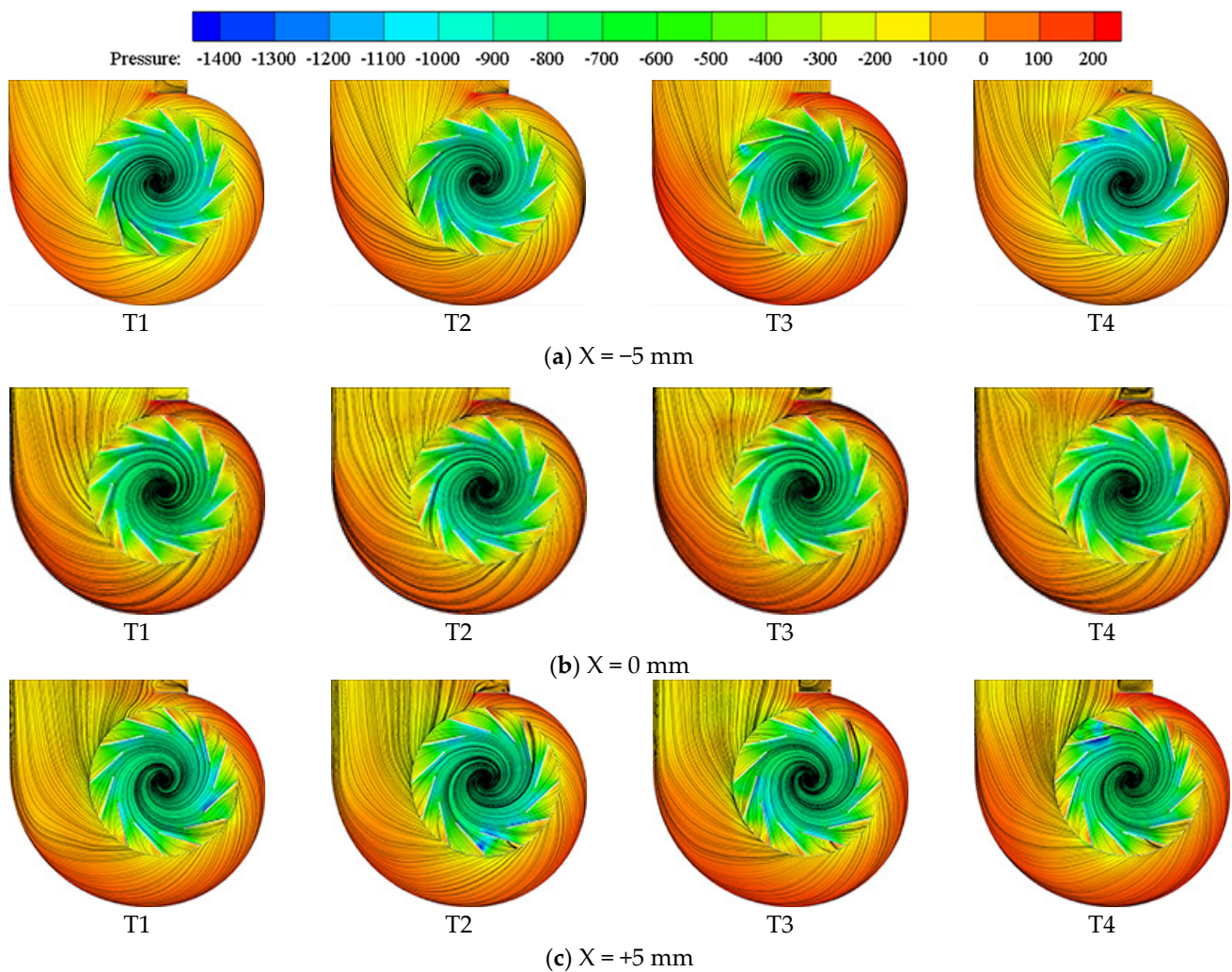


**Figure 11.** Distributions of static pressure and streamlines at four moments for the cross-section at  $Y = 2$  mm.

The flow at the middle constant- $Y$  cross-section ( $Y = 60$  mm) is more affected by the offset impeller, as seen in Figure 12. Separated vortices form on the suction surfaces and near the trailing edge of part of the blades, while the size, number, and position of the vortices depend on the offset distance. In the figure, the size of the vortices is relatively small for the baseline model ( $X = 0$  mm), and the vortices only form in several blade passages under the designed flow rate. However, for the other two modified models with an offset impeller, the size of the separated vortices is larger, which could occupy half or even the whole blade passage, and they move with the rotation of the impeller. The offset impeller also improves the uniformity of flow at the outlet of the volute. The streamlines at the outlet of the baseline model exhibit in-plane motion like secondary flow, while the fluid exits from the volute smoothly for the modified models.

The flow near the shroud of the impeller is the most remarkably affected by the offsetting of the impeller, as shown in Figure 13. Almost all blade passages for the three models are occupied by separated vortices as a result of the transition in the direction of local flow, but the distribution of vortices is different. For the  $X = -5$  mm model, the area of the high-pressure region near the baffle and the number of backflow vortices is larger, indicating that the impeller offsetting in the negative- $X$  direction has a great influence on the flow between the impeller and the baffle. For the  $X = +5$  mm model, the flow through the blade passages near the baffle and the inner side of the volute is better than in the other models. However, there is a large-scale low-pressure area in other blade passages,

and the vortices at the trailing edge of the blade suction surface in this region and the boundary layer separation of the neighboring blade pressure surface are mixed with each other, resulting in a large loss.

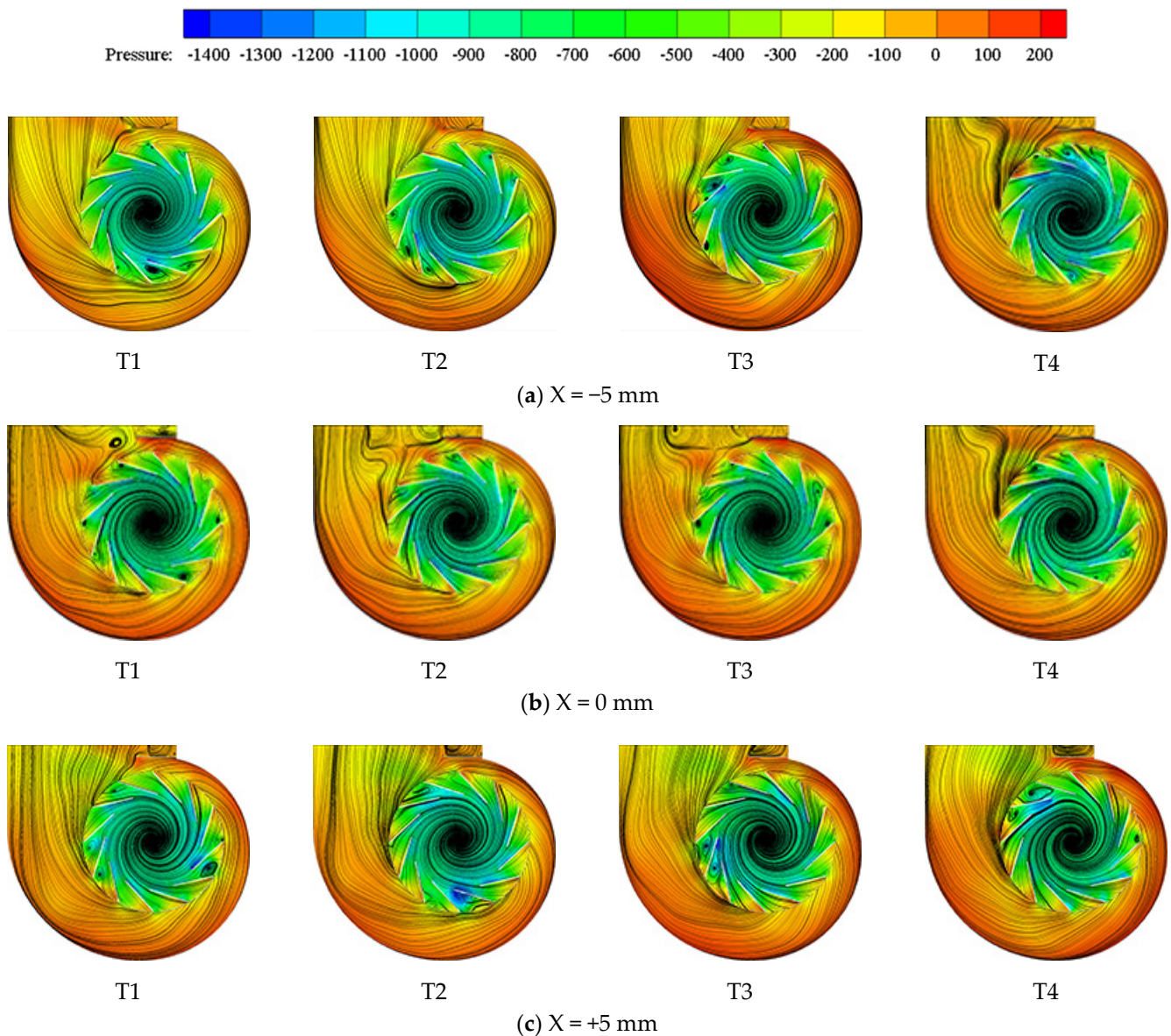


**Figure 12.** Distributions of static pressure and streamlines at four moments for the cross-section at  $Y = 60$  mm.

Comparing the distributions of static pressure and streamlines, it is concluded that the offsetting of the impeller in the negative- $X$  direction (close to the top of the volute) results in blockage in the blade passages near the baffle. However, the offsetting in the positive- $X$  direction (close to the bottom of the volute) generates separated vortices on the pressure surfaces of the blades at the  $Y = 118$  mm cross-section, which deteriorates the flow patterns in the blade passages.

The flow from the beginning to the end of the twelfth revolution of the impeller (36 moments in total) in the multiple blade passages is further quantitatively explored by the velocity field on the  $Y = 2$  mm, 60 mm, and 118 mm cross-sections. Several sampling monitors are set in the blade passages, as shown in Figure 14; the circumferential position of zero degrees is placed near the pressure surface of the blade in the blade passage just off the baffle, and the circumferential distance between two neighboring monitors is  $10^\circ$ . The

radial velocity on these monitors is recorded at the same moment, which is used to analyze the through-flow in the blade passage; it is calculated with a negative value denoting the reversed flow moving in the direction from the outlet to the inlet of the impeller. Moreover, the surface of the volute is also labeled by several notations, i.e.,  $\Phi 1$ ,  $\Phi 2$  and  $\Phi 3$ , for further analysis of the boundary layer flow.

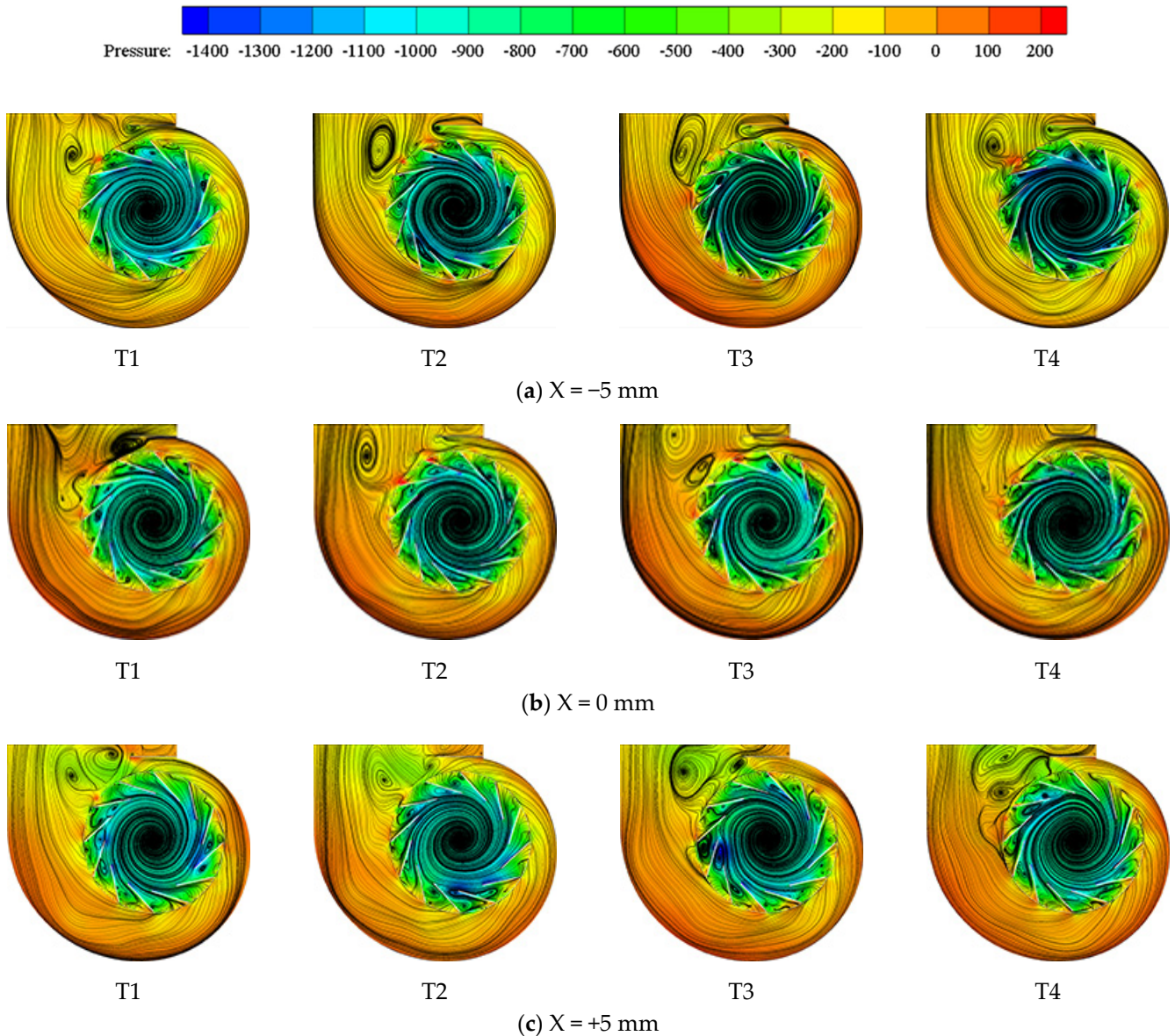


**Figure 13.** Distributions of static pressure and streamlines at four moments for the cross-section at  $Y = 118$  mm.

The circumferential distribution of instantaneous radial velocity obtained on the monitors is presented in Figure 15 for the baseline and modified models. There is no reversed flow with a negative radial velocity on the  $Y = 2$  mm cross-section, and the magnitude of radial velocity is generally uniform in the circumferential direction, especially for the  $X = -5$  mm model. There is fluctuation for the  $X = +5$  mm model in the region  $240\text{--}300^\circ$  as the flow exits from the impeller and is partly blocked by the baffle, which is attributed to the offset impeller in which the baffle blocks a larger part of the blade passages.



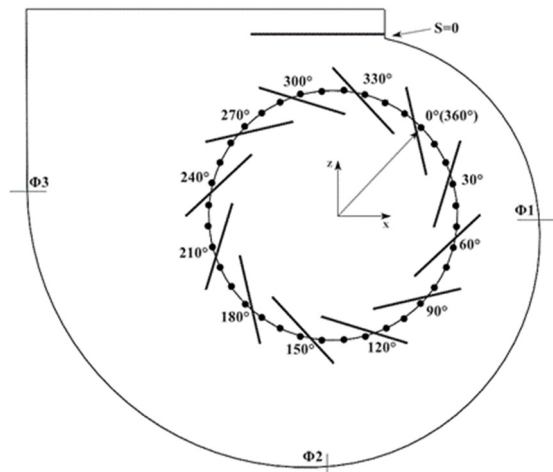


Figure 14. The sampling monitors in the blade passages and on the volute surface.

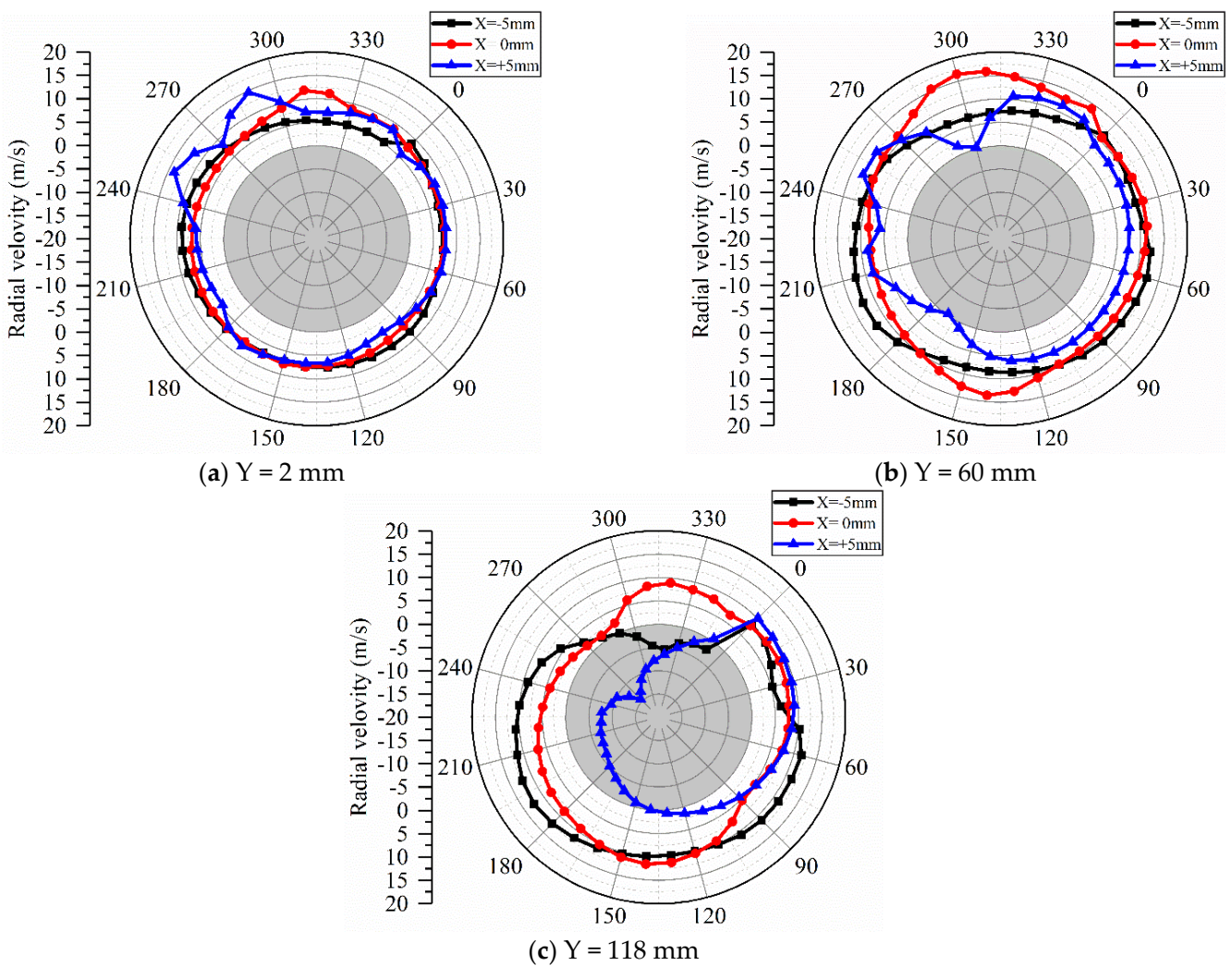


Figure 15. Circumferential distribution of instantaneous radial velocity in the impeller.

The flow is still generally uniform on the  $Y = 60$  mm cross-section, although the circumferential variation of velocity magnitude is larger for all models than for the  $Y = 2$  mm cross-section. As the cross-section is closer to the shroud of the impeller, the height of the baffle is larger and more significantly affects the flow exiting from the impeller. In

the baffle-affected region, the peak value and variation range of the radial velocity of the baseline model fluid become larger. Substantial circumferential variation is observed for the  $X = +5$  mm model; the radial velocity is nearly zero at  $170^\circ$  and  $300^\circ$ , and the local fluctuation is also large in these two intervals.

Strong non-uniform flow is observed on the  $Y = 118$  mm cross-section, as it is closest to the shroud and the flow deviates as it enters the impeller, which is consistent with the observation of Figure 13. Local reversed flow occurs for the two modified models. For the  $X = -5$  mm model, the magnitude of radial velocity starts to decrease around  $250^\circ$ , turns to be strongly negative at  $320^\circ$ , and then rapidly recovers to positive as the local flow is no longer affected by the baffle. The reversed flow is remarkable in both magnitude and range for the  $X = +5$  mm model. The reversed flow occurs in the region  $140\text{--}350^\circ$  and has the highest negative velocity of  $-20$  m/s at the circumferential position of  $270^\circ$ , which is in the blade passage close to the outlet of the volute, as the exiting flow from the impeller is blocked by the baffle.

It is concluded that the offset impeller affects the flow in the blade passages most significantly near the shroud of the impeller, and the influence is notable for the  $X = +5$  mm model, in which the impeller is away from the top of the volute. However, for the  $X = -5$  mm model, the gap between the impeller and baffle is larger, which imposes less resistance on the flow exiting from the impeller; thus, the reversed flow is weak.

The magnitude of instantaneous velocity, as a reflection of the kinetic of the flow, is presented in Figure 16 for its circumferential distribution in the impeller. The flow is still the most uniform on the  $Y = 2$  mm cross-section. The magnitude of velocity for the  $X = +5$  mm model drops sharply near the volute outlet and the baffle-affected area, and the non-uniformity is obvious. The magnitude of velocity reduces for the baseline and  $X = -5$  mm models on the  $Y = 60$  mm cross-section, while a much larger velocity is observed in the  $180\text{--}300^\circ$  region for the  $X = +5$  mm model. The circumferential distribution of velocity magnitude is substantially non-uniform on the  $Y = 118$  mm cross-section for all three models, and the flow for modified models is greatly affected by the baffle as the impeller is offset placed. For the  $X = -5$  mm model, the velocity is largest in the region  $270\text{--}350^\circ$  since the baffle permits the flow exiting from the impeller and the volute with less blockage. However, as the baffle blocks more fluid for the  $X = +5$  mm model, the velocity is the largest, mainly in the region  $150\text{--}230^\circ$  but rapidly reduces as the fluid approaches the outlet of the volute as it is blocked by the baffle.

#### 3.2.4. Flow Patterns on the Blade Surface

The influence of the offset impeller on the boundary layer flow of the blades is presented and analyzed by the distributions of instantaneous static pressure and limiting streamlines on the blade surfaces, as given in Figure 17, in which the color of the streamlines denotes the static pressure.

The separation and non-uniformity of the boundary layer flow is clearly seen. As affected by the baffle, the streamlines on the pressure surface of the blades near the baffle deviate close to the shroud of the impeller for the  $X = -5$  mm and baseline models, while the deviation is minor for the  $X = +5$  mm model, implying a regulated boundary layer flow on the few blades. However, severe separation and local recirculating vortices are found on the blades away from the baffle, especially close to the leading edge of the suction surface, which could extend until the trailing edge, such as the  $X = +5$  mm model. This is attributed to the non-zero flow angle at the inlet of the impeller as a result of the offset impeller and blockage from the collector, which is consistent with the observations in Figures 9 and 13.

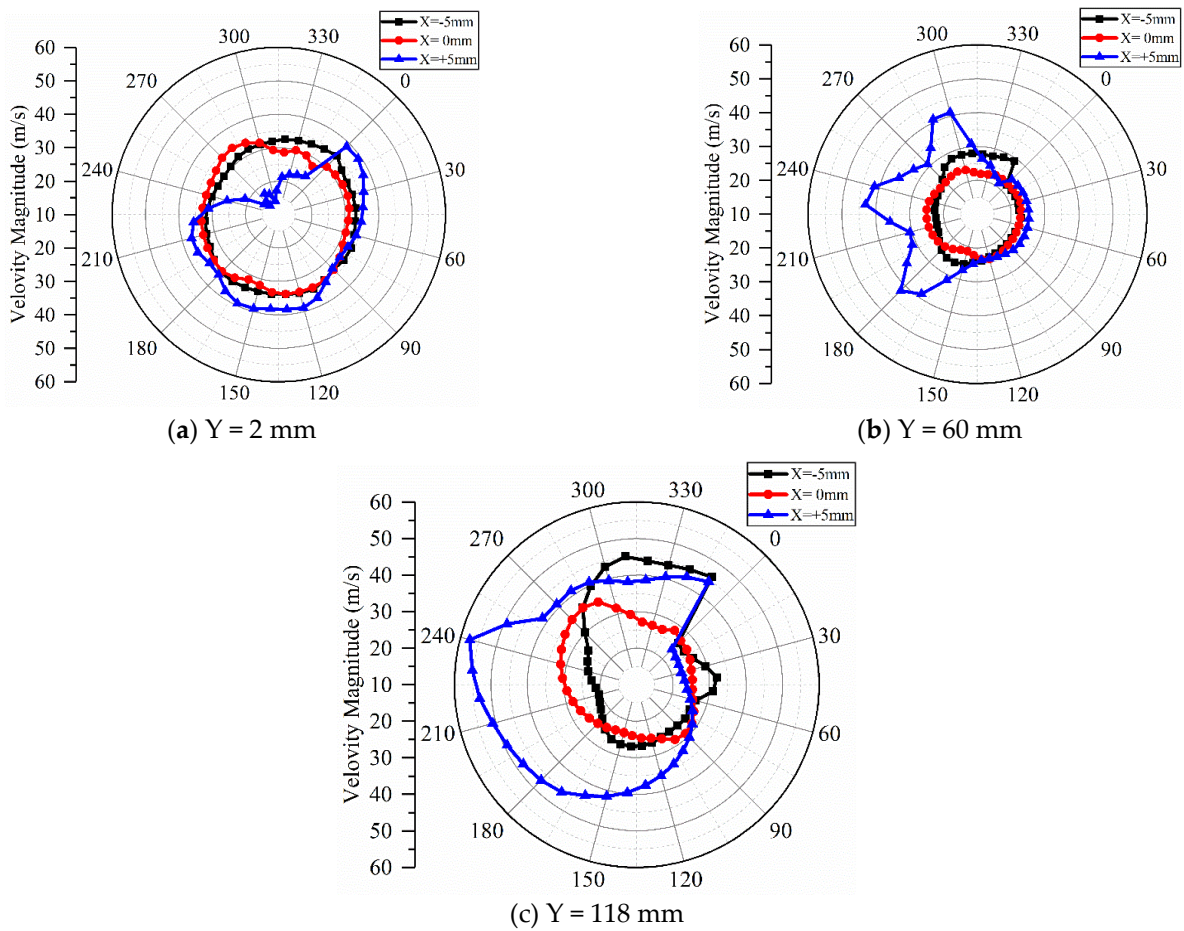


Figure 16. Circumferential distribution of magnitude of instantaneous velocity in the impeller.

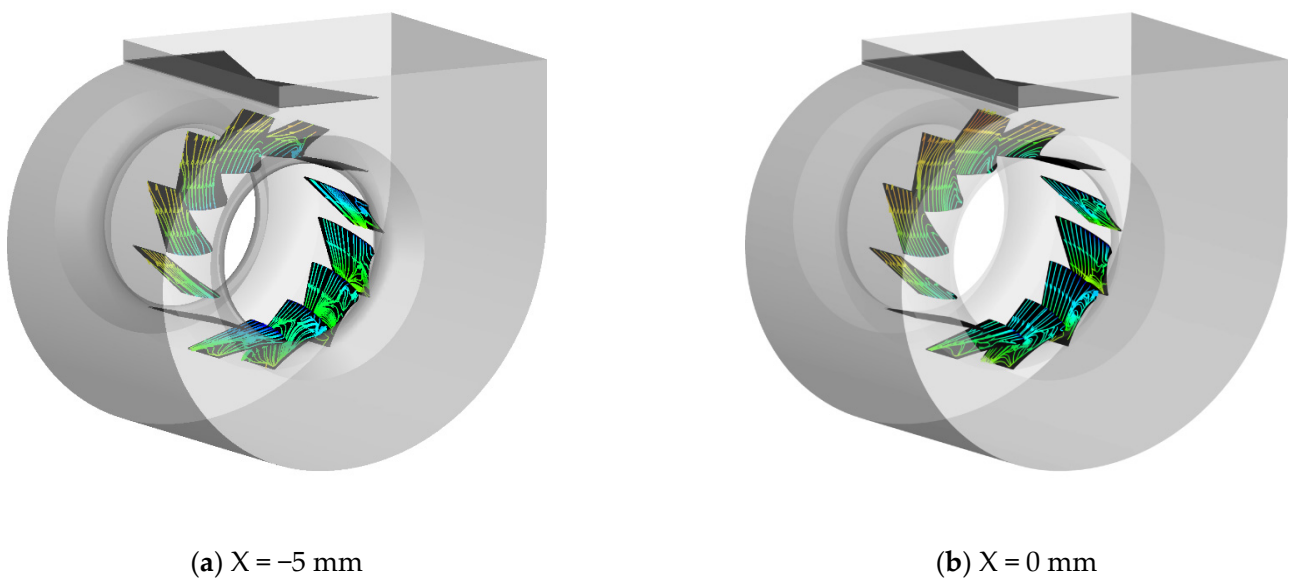
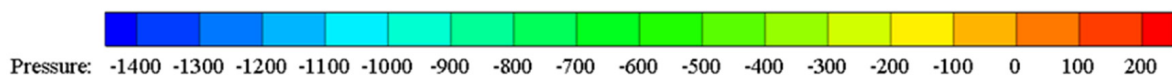
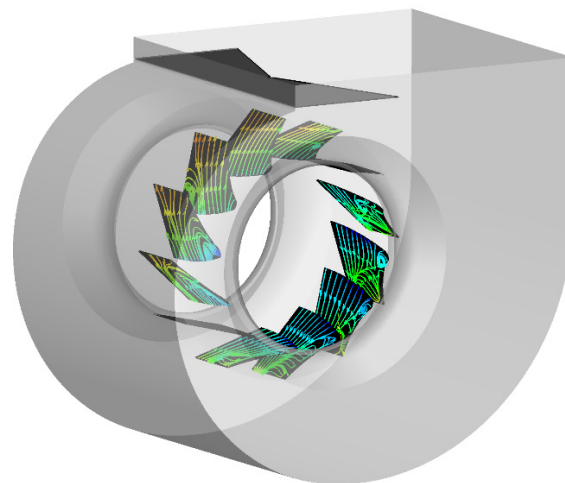


Figure 17. Cont.

(c)  $X = +5$  mm

**Figure 17.** Distributions of static pressure and limiting streamlines on the blade surfaces of the three models.

### 3.3. Flow in the Volute

#### 3.3.1. Flow Patterns within the Volute

The distributions of instantaneous static pressure and streamlines on different constant- $Y$  cross-sections for the several models are given in Figures 11–13. On the  $Y = 2$  mm cross-section close to the central disc of the impeller, the  $X = -5$  mm model reduces the distance between the impeller and the top of the volute, i.e., the impeller is less blocked by the baffle. The fluid exiting from the impeller impinges on the surface of the volute near the outlet, increasing energy loss. The impeller is relatively away from the top surface of the volute for the baseline and  $X = +5$  mm models. The fluid exiting from the impeller has a sufficiently large space to develop and deviate in direction and moves in parallel with the volute surface near the outlet of the volute with less impingement. Recirculating vortices also form outside the baffle.

On the  $Y = 60$  mm cross-section, a large recirculating vortex is generated in the region to the outlet of impeller and besides the baffle for all three models. The size and position of the vortex vary over time but are always noticeable. For the baseline and  $X = +5$  mm models, due to the long distance between the impeller and the volute surface, the kinetic energy of fluid is reduced after impingement of the volute surface near the outlet, and it does not continue to move against the wall but is offset close to the rotation direction of the impeller.

On the  $Y = 118$  mm cross-section close to the shroud of the impeller, the patterns of the recirculating vortex are more complicated. Since the height of the baffle is larger on this cross-section, the area of the volute outlet is small, and the fluid recirculates at the outlet, resulting in a lower static pressure rise for the  $X = -5$  mm model. For the baseline model, in the normal model, a small part of the fluid returns back toward the baffle, and most of the fluid interacts with the fluid at the impeller outlet, forming a vortex at the volute outlet. However, the fluid for the  $X = +5$  mm model does not move back at the baffle, indicating that the offset impeller strengthens the blocking effect of the baffle and effectively reduces the impact of the reversed flow on the performance of the fan.

In conclusion, the  $X = -5$  mm model reduces the area of the volute outlet and weakens the influence of the baffle on outflow; the fluid returns back to the volute and interacts with the internal flow. The offset impeller in the other direction enhances the influence of the baffle and stabilizes the flow near and downstream of the inner side of the baffle.

### 3.3.2. Pressure Fluctuation Inside the Volute

The strength of the transient fluctuation of the internal flow of the volute is quantitatively revealed by the pressure signal. We set four monitors, termed monitor-A–D, on the  $Y = 2$  mm cross-section across the circumference of the outlet of the impeller, as shown in Figure 18. The four monitors are located in the middle of the impeller outlet and the volute surface or baffle. The time history of static pressure is recorded for two revolutions of the impeller and is given in Figure 19, where the vertical line in the figure is the dividing line between the eleventh and twelve revolutions of the impeller. It is seen in the figure that the pressure fluctuation presents similar, but not identical, temporal variations on all monitors, and the pressure fluctuation for the baseline model is smaller than the two modified models with an offset impeller.

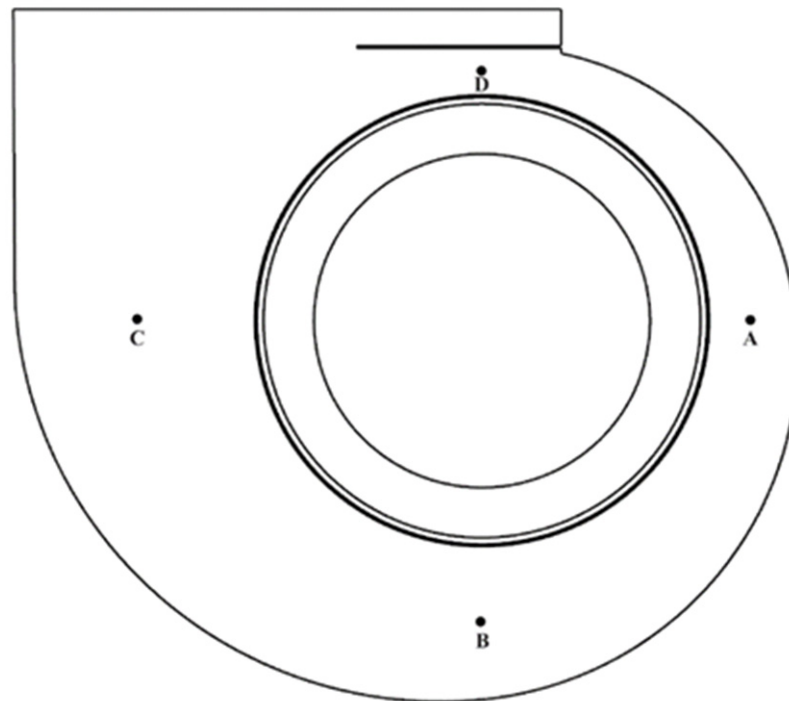
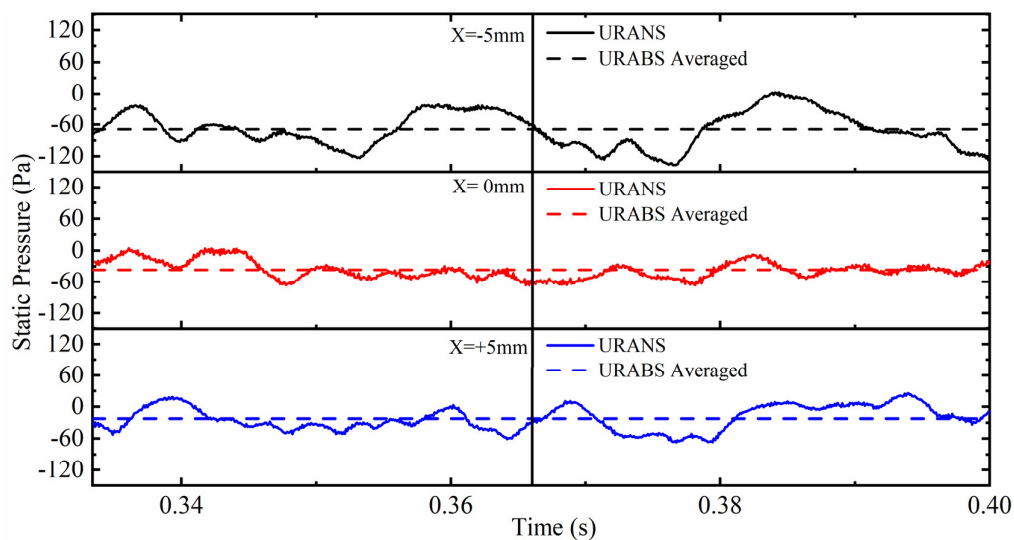
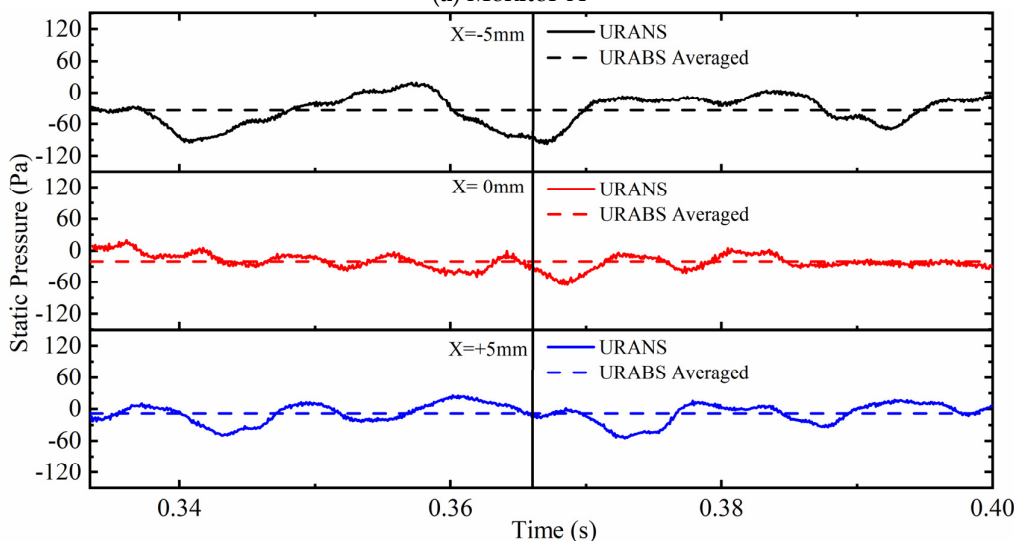


**Figure 18.** Positions for the pressure monitors within the volute.

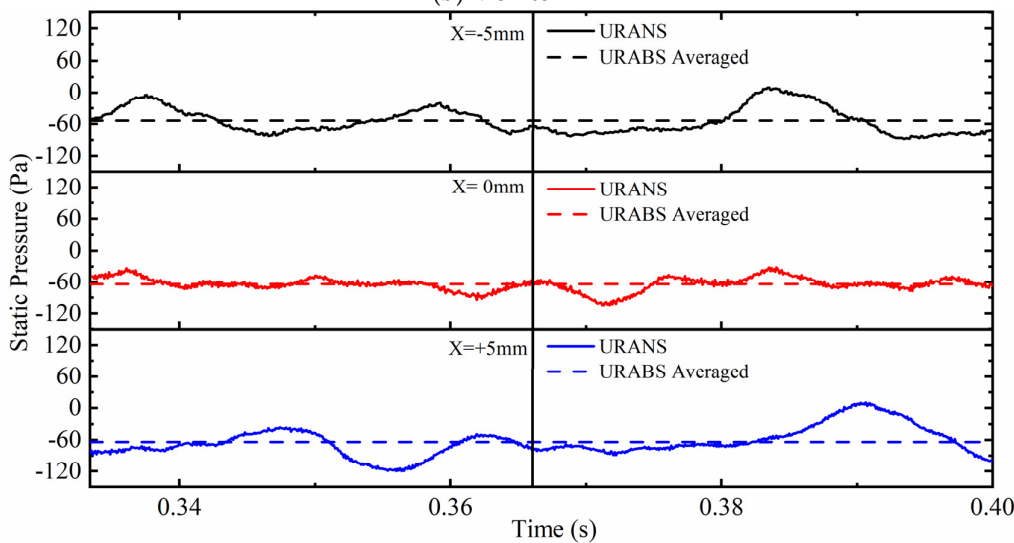
Since the impeller offset with  $X = +5$  mm is closest to the bottom of the volute, the averaged pressure of monitor-A is the highest among the three models, while the magnitude is reduced for the baseline and  $X = -5$  mm models. The influence of the offset impeller on the pressure fluctuation is weakened for monitor-B. For monitor-C since it is located in a large space close to the volute outlet, the offset distance has a minor impact on the averaged pressure and the frequency of fluctuation. The averaged pressure for the offset models is basically the same and is slightly lower than that of the baseline model. The amplitude of pressure fluctuation is the most pronounced for monitor-D since it is located between the impeller and baffle and the gap is narrow in size, especially for the two modified models as a result of the local recirculating flow. The averaged pressure is the highest among the four monitors, but its magnitude is large for the baseline model and is almost the same for the two modified models.



(a) Monitor-A



(b) Monitor-B



(c) Monitor-C

Figure 19. Cont

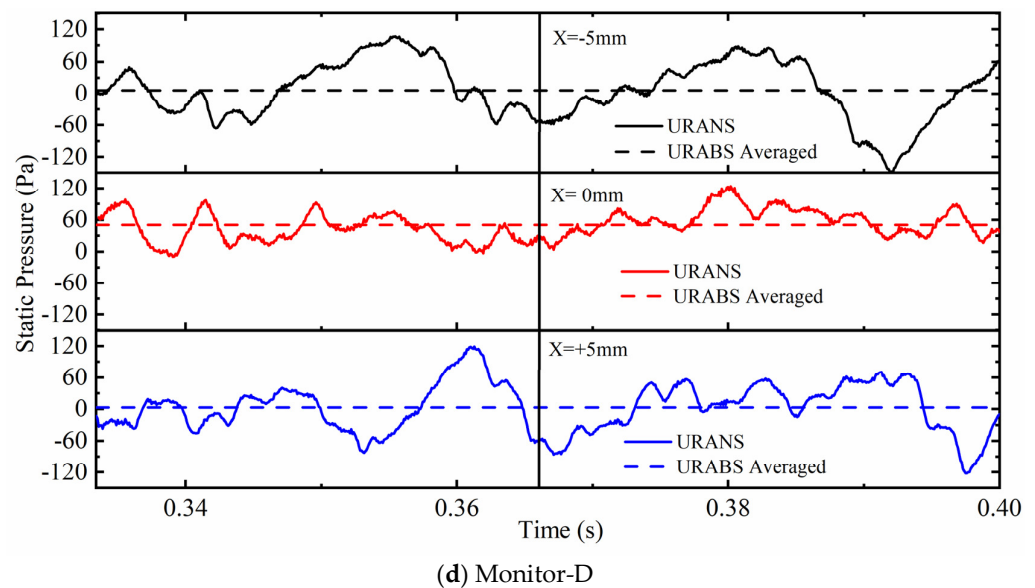


**Figure 19.** Time history of static pressure recorded at the four monitors and its time-averaged value during the two revolutions of the impeller.

### 3.3.3. Boundary Layer Flow on the Volute Surface

The radial distance between the outlet of the impeller and the volute surface changes as the impeller is offset. Although the geometry of the volute remains the same, the boundary layer flow on the surface is consequently affected. Here, we analyze the characteristics of the boundary layer flow of the volute in detail. Since there are two sets of blades in the double-suction centrifugal fan and the blades are installed in a staggered manner, the offset impeller has a different impact on the boundary layer flow. In Figure 20, we present the circumferential distribution of static pressure on the volute surface on the  $Y = \pm 2$  mm,  $\pm 60$  mm, and  $\pm 118$  mm cross-sections. The abscissa of the sub-figure measures the arc length of the volute surface from approximately the position of the baffle, as seen in Figure 14, where the featured circumferential positions  $\Phi 1$ ,  $\Phi 2$  and  $\Phi 3$  are also noted.

Figure 20 shows that the recovery of static pressure is notable for flow at the middle of the impeller and near the shroud. The magnitude of static pressure is generally low for the  $X = -5$  mm model on all three cross-sections and is similar for the baseline and  $X = +5$  mm models. In the region upstream of  $\Phi 1$ , the magnitude of the static pressure varies drastically because the air re-enters the volute through the baffle, indicating that the geometric variation of the volute would have an impact on the boundary layer flow. A local adverse pressure gradient field may form. In the region from  $\Phi 1$  to  $\Phi 2$ , the magnitude of the static pressure does not vary significantly, while it generally starts to decrease around the circumferential position  $\Phi 3$ .

Figure 21 shows the distribution of the skin friction coefficient on the volute surface. In the region upstream of  $\Phi 1$ , obvious differences can be observed because the impeller and the volute surface are close to each other, and the slight change in the distance between the left and right blades and the volute surface will cause the friction coefficient to be different. The  $X = +5$  mm model is close to the impeller and the volute surface, and the volute surface has a strong diffusion effect, so the skin friction coefficient is larger than in other models. For the  $X = -5$  mm model, at section  $Y = -118$  mm of the left volute, the skin friction coefficient first rises and then falls, forming a peak value, and the friction coefficient reaches 5.5. In the region between  $\Phi 1$  and  $\Phi 3$ , the several curves are generally consistent in the majority region, and the friction coefficients of the left and right cross-sections remain low and change gently. At  $\Phi 3$ , the skin friction coefficient for the  $X = -5$  mm model is much higher than the other two models on the  $Y = +60$  mm and  $Y = +118$  mm cross-sections, and then there is a significant decrease trend at the volute outlet. This is because the offset of the impeller to the volute surface causes the air to collide with the volute surface in

advance, causing the wall pressure to increase, and then the air close to the wall flow gradually decreases.

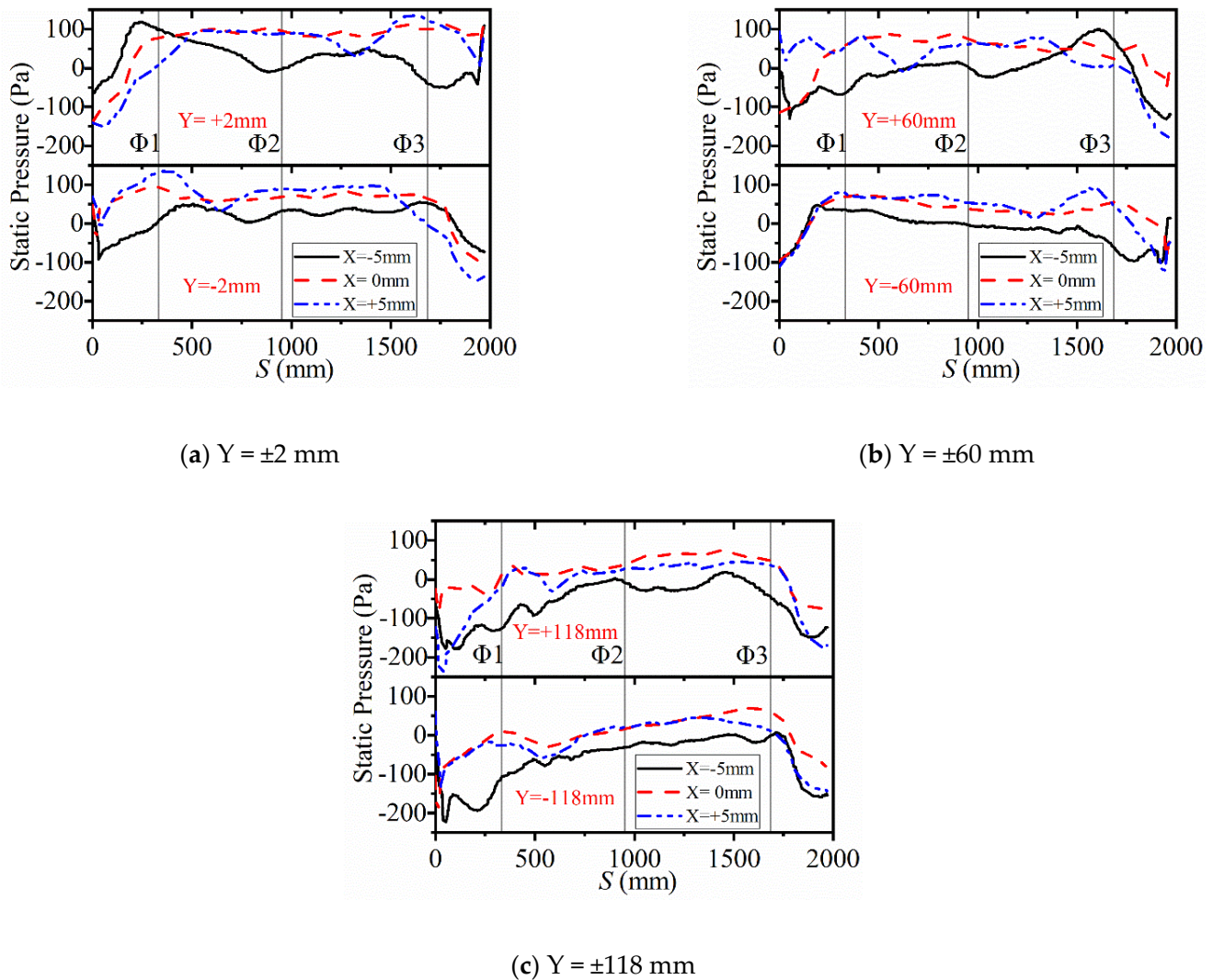


**Figure 20.** Distribution of static pressure on the whole circumferential surface of the volute at different constant-Y cross-sections.

### 3.4. Unsteady Flow around the Baffle

#### 3.4.1. Static Pressure Distribution of Inside Baffles

From the above analysis, it can be found that the impeller offset has a great influence on the flow around the outlet of the volute and baffle, especially on their inner surfaces. Since the radial offset of the impeller changes the influence range of the baffle, the fluid collides with the baffle in advance or later, resulting in a complex flow in this region and uneven pressure distribution.

Figure 22 shows the distribution of static pressure on the inner surface of the baffles. The fluctuations in the pressure distribution are mainly concentrated in the region affected by the impeller blades, that is, between the sections  $Y = -118 \text{ mm}$  and  $Y = +118 \text{ mm}$ . The averaged pressure in this region is the largest, and two peaks of symmetrical distribution appear. The pressure changes on both sides of the baffle are gentle, indicating that the shroud of the impeller has little influence on the pressure of the baffle.



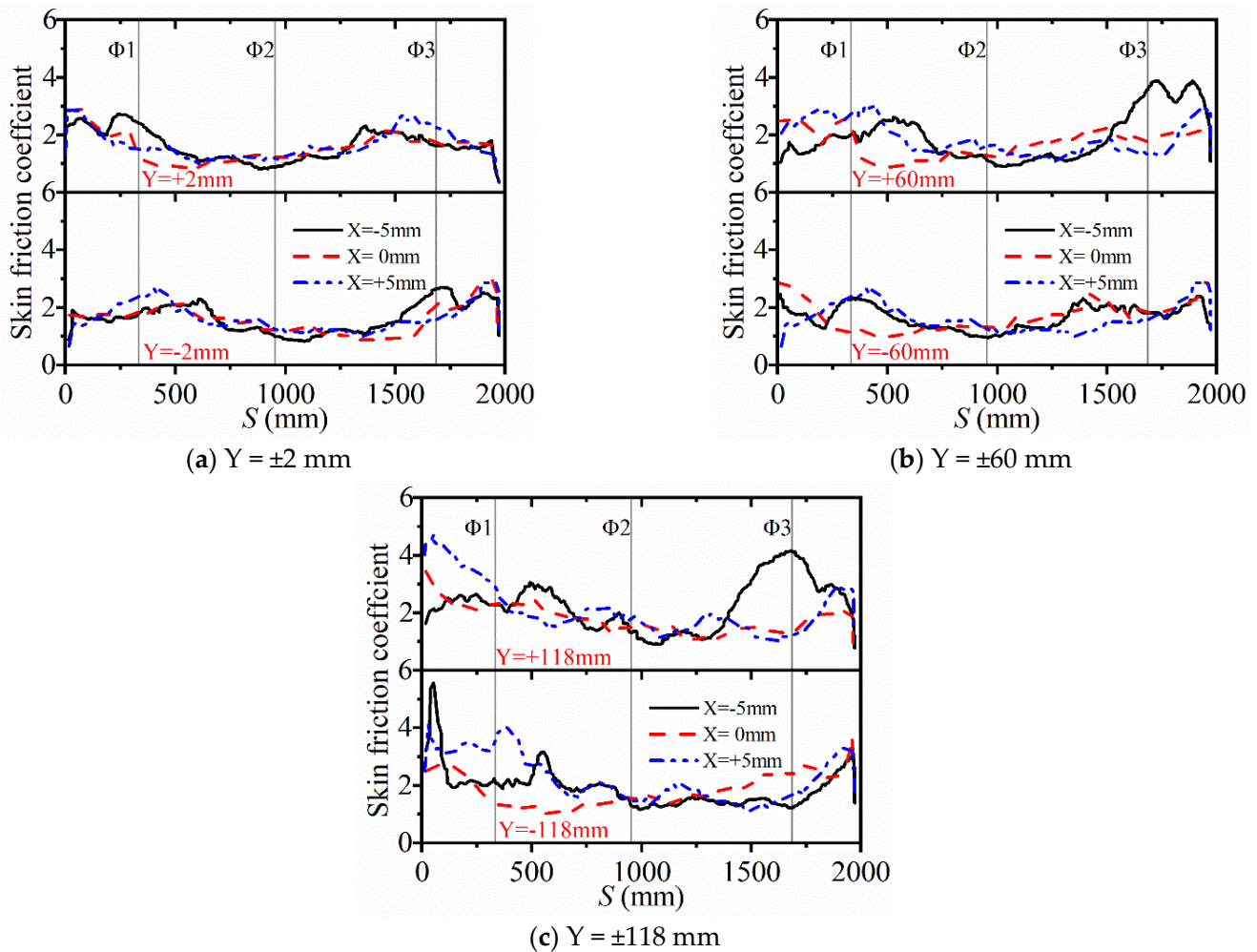


**Figure 21.** The distribution of the skin friction coefficient  $C_f$  on the whole circumferential wall of the volute with different Y planes.

Compared with the baffle of the baseline model, for the  $X = -5$  mm model, since the fluid outside the baffle returns back to the volute on the  $Y = 118$  mm cross-section, the pressure inside the baffle has a valley value of all four moments, and the pressure is much smaller in magnitude than the other two models. The positions for the minimum and maximum pressures are very close to each other and change drastically over time. For the  $X = +5$  mm model, the pressure distribution of the baffle is more uniform than in the baseline model, and the maximum value is smaller, indicating that the fluid will flow in the direction of the rotation of the impeller and directly enter the next flow cycle without colliding with the baffle, which is conducive to the flow.

### 3.4.2. Pressure Fluctuations of the Inside Baffle

The baffle blocks the direct outflow of fluids that have not undergone the volute's diffusing action and makes the fluid enter the volute for circulation. Figure 23 shows the time history of the surface-averaged force acting on the inner side of the baffle in the normal direction during one revolution of the impeller. It can be seen more intuitively that the force on the baffle of the baseline model is greater than that of the two modified models. The  $X = -5$  mm model receives the maximum force as the impeller rotates to  $180^\circ$  (moment T3), and then the force drop caused by the reversed flow decreases to a minimum at  $280^\circ$ , indicating that the reversed flow mainly occurs between moments T3 and T4. For the  $X = -5$  mm model, since the impeller is offset to the inner side of the volute, part of the fluid moves directly into the circulation so that the amplitude of force pulsation is small.

The difference between the minimum and maximum values is not significant, which is consistent with the conclusion of the above contour.

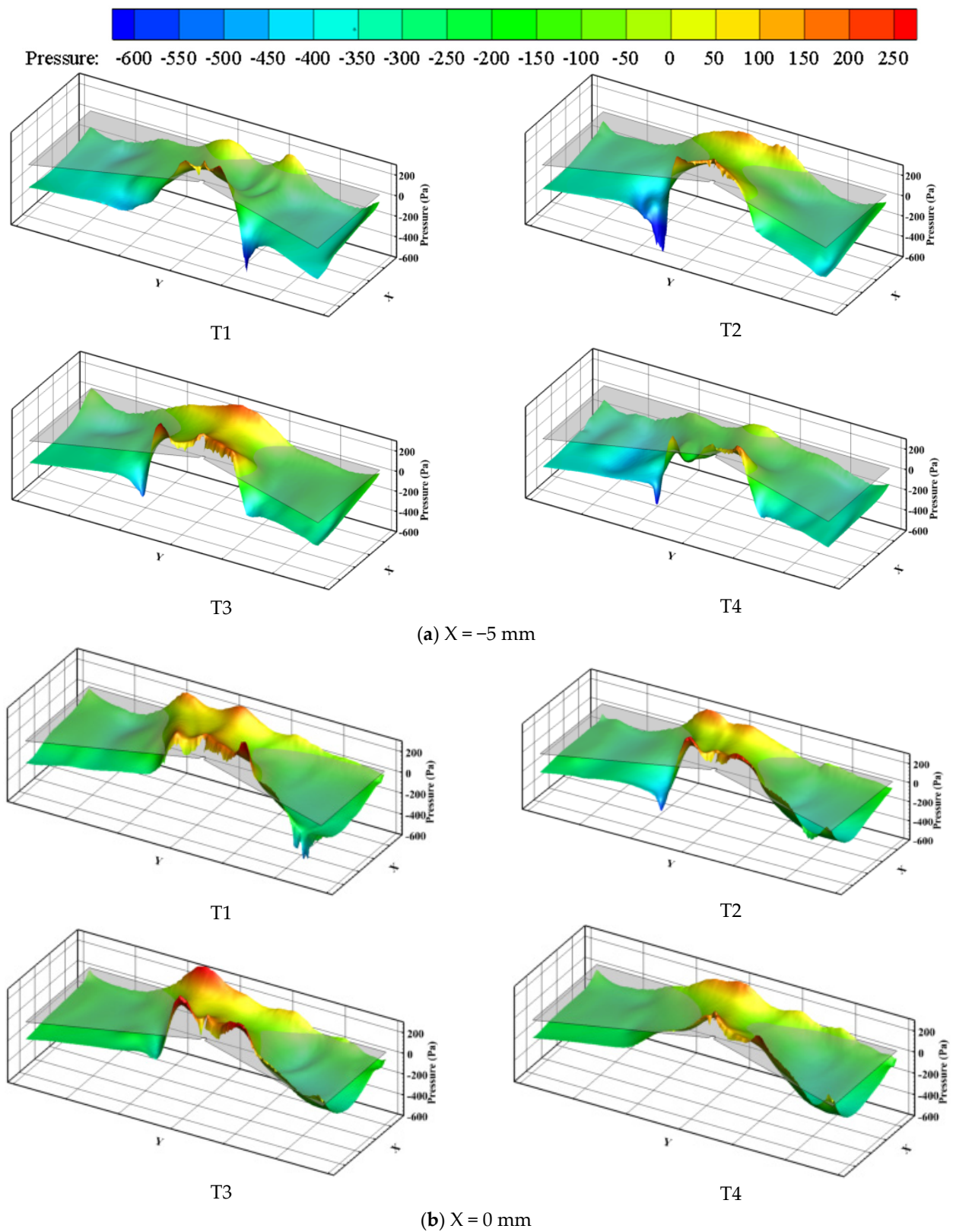
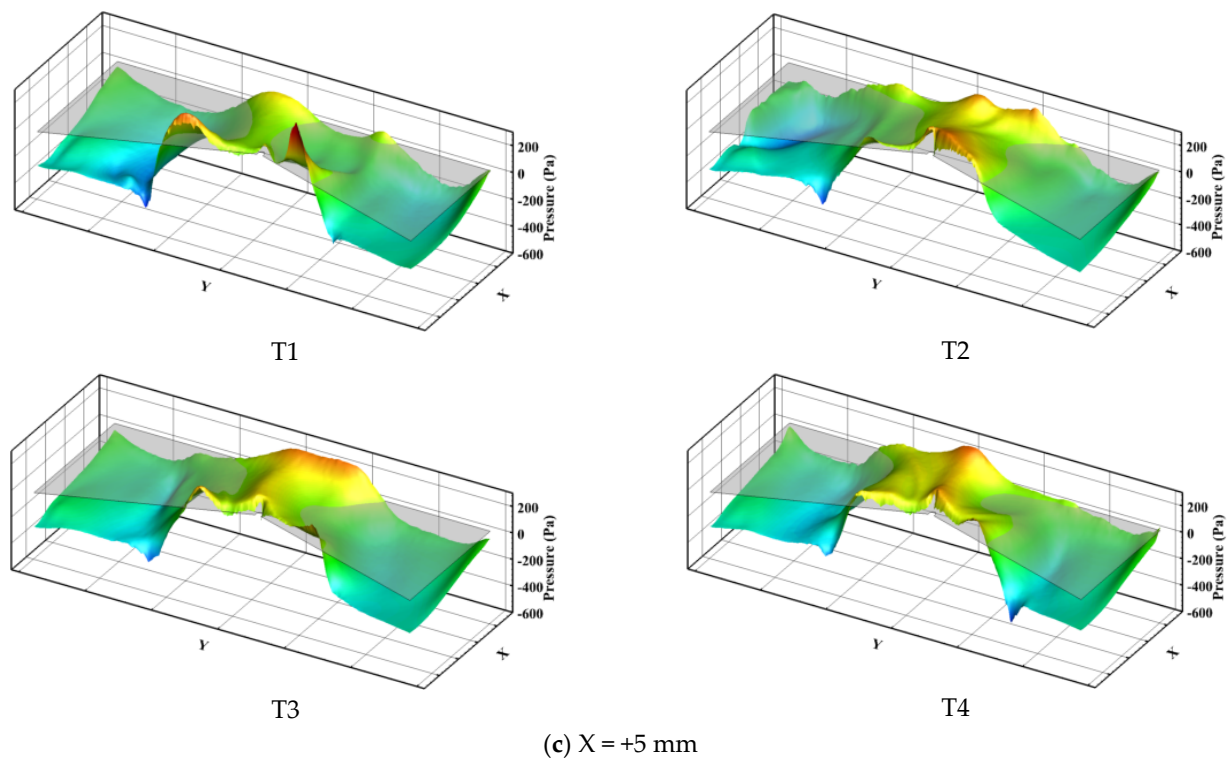
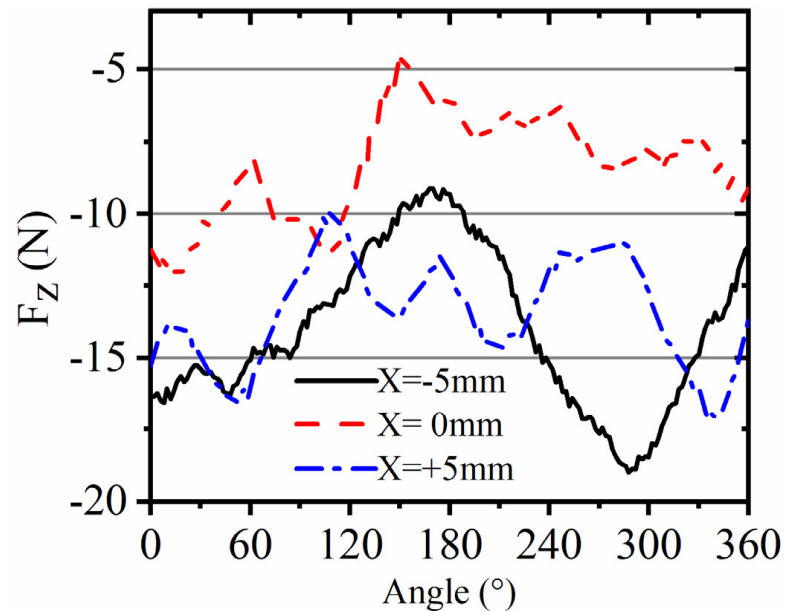


Figure 22. Cont.



**Figure 22.** The static pressure distribution of the inside baffles of the three groups of models at each time.



**Figure 23.** Average force pulsation curve of the inside baffle.

### 3.4.3. Flow Outside of the Volute

As shown in Figure 24, 100 sections perpendicular to the fluid flow direction were taken from the start to the end of the fan outlet domain of 2500 mm. Take the average pressure of each section to analyze the change in the average pressure in the outlet pipe along the flow direction, as shown in Figure 25.

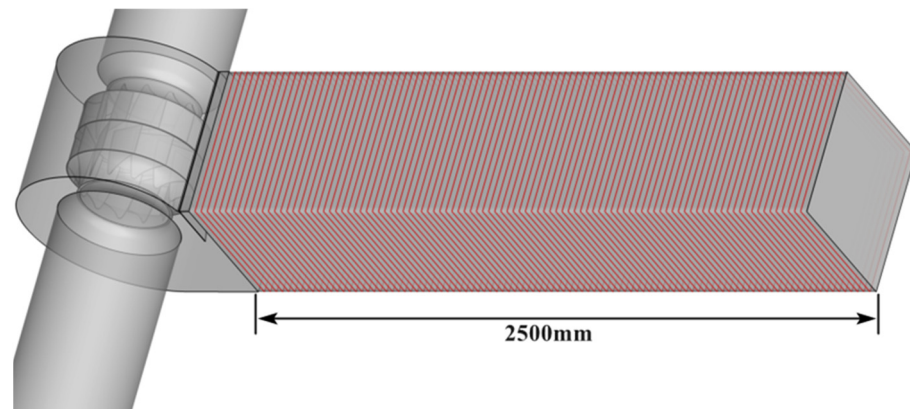


Figure 24. Section division of the outlet domain.

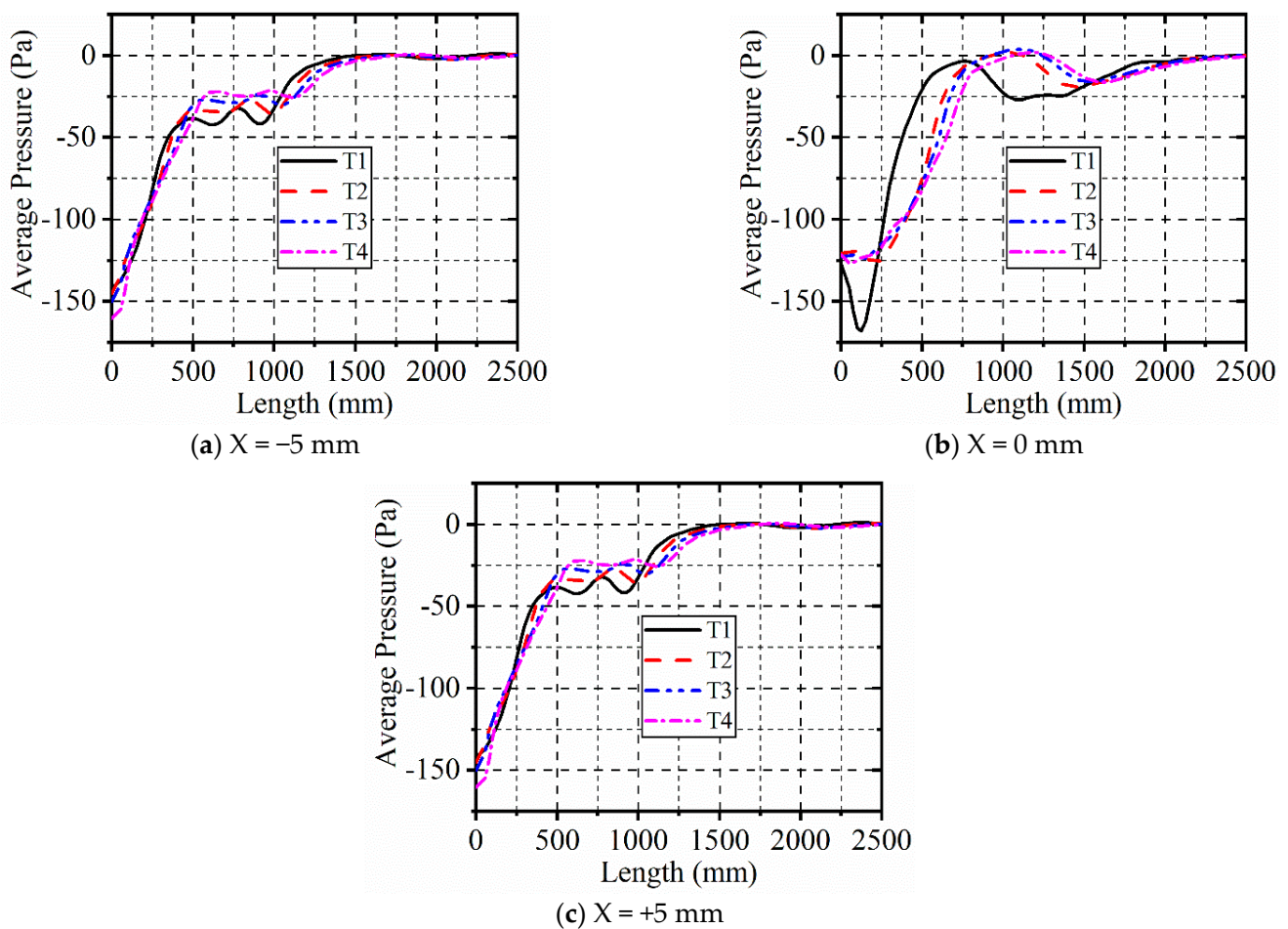


Figure 25. The distribution of surface-averaged static pressure along the outflow domain.

In the initial section of the outlet, the surface average pressure of the normal and offset  $X = +5$  mm models is  $-120$  Pa at the beginning of the outlet. The average surface pressure at this position of the model with offset  $X = -5$  mm is only  $-150$  Pa, which indicates that the backflow at the volute outlet caused by the  $X$  negative offset of the impeller will reduce the pressure at the volute outlet.

In the middle section of the outlet domain, the average pressure of the middle section varies greatly at different times, and the unsteady characteristics are significant. The average pressure of the normal model shows a parabolic trend, first rising and then falling in this area. The model with offset  $X = -5$  mm fluctuates up and down around  $-20$  Pa and

the pressure rises slowly, indicating that the secondary flow movement is complex and the efficiency of converting dynamic pressure into static pressure is low. The model with offset  $X = +5$  mm showed a fluctuating upward trend in the middle section.

At the end of the outlet, the surface pressure of the two groups of offset models basically reaches 0 and does not change, while the normal model still rises slightly, and part of the dynamic pressure is converted into static pressure, which improves the static pressure efficiency of the fan.

#### 4. Conclusions

This work presents a numerical investigation of the influence of a radially offset impeller on the aerodynamic performance and characteristics of the internal flow of a double-suction centrifugal fan. The impeller of the fan is offset from its baseline position; thus, the incoming flow of the impeller is affected by the interaction between the impeller and collector and further affects the flow in the impeller, volute, and even outside of the volute. The conclusions are drawn:

- (1) The minor offset of the impeller lowers the efficiency of the fan to varying degrees. The static pressure efficiency of the fan with an offset impeller of  $X = -5$  mm and  $X = +5$  mm is reduced by 4.04% and 3.75%, respectively.
- (2) The gap between the shroud of the impeller and the collector is changed by the offset impeller, causing uneven distributions of pressure and axial velocity at the inlet of the impeller, and reversed flow occurs in the gap region.
- (3) The pressure fluctuation in the impeller and volute is enhanced by the offset impeller. The offset in the positive X-direction is beneficial for increasing the diffusing effect of the volute, while the offset in the negative X-direction has the opposite effect.
- (4) For the  $X = -5$  mm model, the fluid reverses near the baffle due to the large volute openness, causing increased pressure fluctuation near the baffle. The limiting streamline on the pressure surface of the blades near the baffle is curved, and the area of reversed flow at the trailing edge of the suction surface is large, which lowers the efficiency of the fan.
- (5) For the  $X = +5$  mm model, the velocity of flow around the baffle increases and inhibits the generation of a local recirculating flow. However, the offset impeller reduces the flow angle at the inlet of the impeller, resulting in the generation of a large number of recirculating vortices on the pressure surface of the blade, and the blockage in the blade passages is responsible for the decreased efficiency.

**Author Contributions:** Conceptualization, Z.C. and W.Z.; Data curation, Z.C.; Formal analysis, Z.C.; Funding acquisition, H.Y., P.Y. and W.Z.; Investigation, Z.C. and W.Z.; Methodology, Z.C.; Resources, H.H., C.Z., T.N. and W.Z.; Software, Z.C.; Validation, Z.C., H.H. and W.Z.; Visualization, Z.C.; Writing—original draft, Z.C.; Writing—review & editing, Y.W. and W.Z. All authors have read and agreed to the published version of the manuscript.

**Funding:** This work was supported by the National Natural Science Foundation of China (52176047), the Zhejiang Public Welfare Project (LGG21E060003, LGG20E060001), and the Zhejiang Province Science and Technology Plan Project (2020C04011, 2021C01049).

**Conflicts of Interest:** The authors declare no conflict of interest.

#### References

1. Wang, Y.; Dong, Q.; Zhang, Y. Meridional shape design and the internal flow investigation of centrifugal impeller. *Proc. Inst. Mech. Eng. Part C J. Mech. Eng. Sci.* **2016**, *231*, 4319–4330. [[CrossRef](#)]
2. Li, C.X.; Wang, S.L.; Jia, Y.K. The performance of a centrifugal fan with enlarged impeller. *Energy Convers. Manag.* **2011**, *52*, 2902–2910. [[CrossRef](#)]
3. Younsi, M.; Bakir, F.; Kouidri, S.; Rey, R. Influence of Impeller Geometry on the Unsteady Flow in a Centrifugal Fan: Numerical and Experimental Analyses. *Int. J. Rotating Mach.* **2007**, *2007*, 034901. [[CrossRef](#)]
4. Ding, H.C.; Chang, T.; Lin, F.Y. The influence of the blade outlet angle on the flow field and pressure pulsation in a centrifugal fan. *Processes* **2020**, *8*, 1422. [[CrossRef](#)]

5. Song, Y.; Fan, H.G.; Zhang, W.; Xie, Z.F. Flow characteristics in volute of a double-suction centrifugal pump with different impeller arrangements. *Energies* **2019**, *12*, 669. [CrossRef]
6. Liu, X.M.; Dang, Q.; Xi, G. Performance improvement of centrifugal fan by using CFD. *Eng. Appl. Comput. Fluid Mech.* **2014**, *2*, 130–140. [CrossRef]
7. Jiang, B.; Wang, J.; Yang, X.; Wang, W.; Ding, Y. Tonal noise reduction by unevenly spaced blades in a forward-curved-blades centrifugal fan. *Appl. Acoust.* **2019**, *146*, 172–183. [CrossRef]
8. Madhwesh, N.; Vasudeva Karanth, K.; Yagnesh Sharma, N. Effect of innovative circular shroud fences on a centrifugal fan for augmented performance—A numerical analysis. *J. Mech. Sci. Technol.* **2018**, *32*, 185–197. [CrossRef]
9. Ye, J.J.; Liu, W.W.; Duan, P.; Huang, X.Y.; Shao, J.D.; Zhang, Y. Investigation of the performance and flow behaviors of the multi-blade centrifugal fan based on the computer simulation technology. *Wirel. Pers. Commun.* **2018**, *103*, 563–574. [CrossRef]
10. Velarde-Suañez, S.; Ballesteros-Tajadura, R.; Santolaria-Morros, C.; González-Peñalver, J. Unsteady flow pattern characteristics downstream of a forward-curved blades centrifugal fan. *J. Fluids Eng.* **2001**, *123*, 265–270. [CrossRef]
11. Lee, Y.T. Impact of fan gap flow on the centrifugal impeller aerodynamics. *J. Fluids Eng.* **2010**, *132*, 91103. [CrossRef]
12. Myung, H.J.; Baek, J.H. Mean velocity characteristics behind a forward-swept axial-flow fan. *JSME Int. J. Ser. B* **1999**, *42*, 476–488. [CrossRef]
13. Zhu, G.J.; Bo, X.Y.; Feng, J.J.; Wu, G.K. Effect of clearance jet on aerodynamic performance of centrifugal fan. *IOP Conf. Ser. Mater. Sci. Eng.* **2019**, *657*, 012003. [CrossRef]
14. Fukutomi, J.; Kuwauchi, T.; Itabashi, A.; Nakase, Y.; Kuwada, T. A Study of Sirocco Fan with Eccentric Inlet Nozzle. *Trans. Jpn. Soc. Mech. Eng. Ser. B* **1999**, *65*, 2023–2029. [CrossRef]
15. Liu, H.; Jiang, B.Y.; Wang, J.; Yang, X.P.; Xiao, Q.H. Numerical and experimental investigations on non-axisymmetric D-type inlet nozzle for a squirrel-cage fan. *Eng. Appl. Comput. Fluid Mech.* **2021**, *15*, 363–376. [CrossRef]
16. Zhou, S.Q.; Wang, M.; Li, Z.Y.; Zhang, S.C. Influence of volute retrofit design on performance of multi-blade centrifugal fan. *Trans. Chin. Soc. Agric. Mach.* **2018**, *49*, 180–186. [CrossRef]
17. Pan, D.; Whitfield, A.; Wilson, M. Design considerations for the volutes of centrifugal fans and compressors. *Proc. Inst. Mech. Eng. Part C J. Mech. Eng. Sci.* **2016**, *213*, 401–410. [CrossRef]
18. Yang, X.; Chen, W.M.; Yuan, M.J.; Wen, X.F.; He, M.J. Experimental study on the effect of relative impeller-to-volute position on the performance of multi-blade centrifugal fan. *Fluid Mach.* **2011**, *39*, 1–5. [CrossRef]
19. Wang, Z.; Xi, G.; Liu, Q. Aerodynamic effects of impeller-diffuser axial misalignment in low-flow-coefficient centrifugal compressor. *Sci. China Technol. Sci.* **2014**, *58*, 29–36. [CrossRef]
20. Baun, D.O.; Köstner, L.; Flack, R.D. Effect of relative impeller-to-volute position on hydraulic efficiency and static radial force distribution in a circular volute centrifugal pump. *J. Fluids Eng.* **2000**, *122*, 598–605. [CrossRef]
21. Younsi, M.; Bakir, F.; Kouidri, S.; Rey, R. Numerical and experimental study of unsteady flow in a centrifugal fan. *Proc. Inst. Mech. Eng. Part A J. Power Energy* **2007**, *221*, 1025–1036. [CrossRef]
22. Ding, J.; Du, X.; Zhang, L.X. Investigation of the effect of volute openness on aerodynamic characteristics of a centrifugal fan. *Compress. Blower Fan Technol.* **2012**, *5*, 22–26. [CrossRef]
23. Li, Z.H.; Ye, X.X.; Wei, Y.K. Investigation on vortex characteristics of a Multi-Blade centrifugal fan near volute outlet region. *Processes* **2020**, *8*, 1240. [CrossRef]
24. Zhang, J.H.; Chu, W.L.; Zhang, H.G.; Wu, Y.H.; Dong, X.J. Numerical and experimental investigations of the unsteady aerodynamics and aero-acoustics characteristics of a backward curved blade centrifugal fan. *Appl. Acoust.* **2016**, *110*, 256–267. [CrossRef]
25. Wu, L.M.; Liu, X.M.; Wang, M.H. Effects of Bionic Volute Tongue on Aerodynamic Performance and Noise Characteristics of Centrifugal Fan Used in the Air-conditioner. *J. Bionic Eng.* **2020**, *17*, 780–792. [CrossRef]
26. Dong, R.; Chu, S.; Katz, J. Effect of modification to tongue and impeller geometry on unsteady flow, pressure fluctuations, and noise in a centrifugal pump. *J. Turbomach.* **1997**, *119*, 506–515. [CrossRef]
27. González, J.; Parrondo, J.; Santolaria, C.; Blanco, E. Steady and unsteady radial forces for a centrifugal pump with impeller to tongue gap variation. *J. Fluids Eng.* **2006**, *128*, 454–462. [CrossRef]
28. Lv, Y.K.; Zhang, B.; Cheng, B. The optimal research on impeller central location of centrifugal fan. *Appl. Mech. Mater.* **2014**, *668*, 729–732. [CrossRef]
29. Patil, S.R.; Chavan, S.T.; Jadhav, N.S.; Vadgeri, S.S. Effect of volute tongue clearance variation on performance of centrifugal blower by numerical and experimental analysis. *Mater. Today Proc.* **2018**, *5*, 3883–3894. [CrossRef]
30. Jin, J.M.; Jung, K.J.; Kim, Y.H.; Kim, Y.J. Effects of gap between impeller and volute tongue on a pressure fluctuation in double-suction pump. *J. Mech. Sci. Technol.* **2020**, *34*, 4897–4903. [CrossRef]
31. Menter, F.R.; Kuntz, M.; Langtry, R. Ten years of industrial experience with the SST turbulence model. *Turbul. Heat Mass Transf.* **2003**, *4*, 625–632. Available online: <https://www.researchgate.net/publication/228742295> (accessed on 16 July 2014).
32. Menter, F.R. Influence of freestream values on k-omega turbulence model predictions. *AIAA J.* **1992**, *30*, 1657–1659. [CrossRef]
33. Menter, F.R. Two-equation eddy-viscosity turbulence models for engineering applications. *AIAA J.* **1994**, *32*, 1598–1605. [CrossRef]